 doi:10.20944/preprints201608.0202.v2

Article

Remote sensing and data mining techniques for assessing the urban fabric vulnerability to heat waves and UHI.

Flavio Borfecchia[1]*, Vittorio Rosato[2], Emanuela Caiaffa[2], Maurizio Pollino[2], Luigi De Cecco[1], Luigi La Porta[2], Simone Ombuen[3], Lorenzo Barbieri[3], Federica Benelli[3], Flavio Camerata[3], Valeria Pellegrini[3], Andrea Filpa[3].

[1] ENEA-SSTP-PROTER-OAC (Sustainability of Productive and Territorial systems Dep., Protection and valorization of territory and natural heritage Div., Earth & Climate Observation and Analysis Lab.) ;
[2] ENEA-DTE-SEN-APIC (Energy Technologies Dep. , Smart Energy Div., Analysis and Protection of Critical Infrastructures Lab.) ;
ENEA – Italian National Agency for New Technologies, Energy and Sustainable Economic Development.
C.R. Casaccia – via Anguillarese, 301, Rome – Italy

[3] University Roma Tre – Architecture Department, via della Madonna dei Monti, 40, Rome – Italy.

* Correspondence: flavio.borfecchia@enea.it; Tel.: +39-6-30486042

Abstract: Densely urbanized areas, with a low percentage of green vegetation, due to ongoing Climate Change (CC), are highly exposed to Heat Waves (HW) which nowadays are increasing in terms of frequency and intensity also in the middle-latitude regions. Their negative effects may combine with those of the UHI (Urban Heat Island), a local phenomenon where air temperatures in the compact built up cores of towns increase more than those in the surrounding rural areas, with significant impact on the quality of urban environment, on citizens health and energy consumption, as it has occurred in the summer of 2003 on France and Italian central-northern areas. In this context this work aims at designing and developing a methodology based on aero-spatial remote sensing (EO) at medium-high resolution and most recent GIS techniques, for the extensive characterization of the urban fabric response to these climatic impacts related to the temperature within the general framework of supporting local and national strategies and policies of adaptation to CC. Due to its extension and variety of built-up typologies, the municipality of Rome was selected as test area for the methodology development and validation. First of all, we started by operating through photointerpretation of cartography at detailed scale (1: 5000) on a reference area consisting of a transect of about 20x5 km, extending from the downtown to the suburbs and including all the built-up classes of interest. The reference built-up vulnerability classes found inside the transect were then exploited as training set for their automatic detection over the entire territory of Rome municipality using the satellite EO HR (High Resolution) multispectral data, provided by the Landsat 7 ETM+ sensor, through on purpose developed supervised object classification procedure based on data mining techniques. A preliminary radiometric preprocessing for removing the atmospheric noises and for extracting suitable variables more linked to built-up features and ground surfaces physical properties relevant in urban radiative balance was applied. The classification results were then exploited for implementing a calibration method, based on a typical UHI temperature distribution, derived from MODIS satellite sensor LST (Land Surface Temperature) data of the summer 2003, to obtain an analytical expression of the vulnerability model, previously introduced on a semi-empirical basis.

 doi:10.20944/preprints201608.0202.v2

Keywords: HR Satellite Remote Sensing; Urban Fabric Vulnerability; UHI & Heat Waves; Landsat & MODIS sensors; LST & Urban heating; Segmentation & Objects Classification; Data Mining; Feature extraction & selection; Stepwise regression & model calibration;

PACS: J0101

1. Introduction

The urban heating and the formation of the UHI are typical features of the current urban land transformation with built-up, sailed soils and infrastructures concentration involving modifications of biophysical parameters linked to local atmospheric interactions, heat storage, radiative exchanges and hydrologic balance. The consequent effects are increasingly impacting on environment quality, human health, ecosystem function, local weather and, possibly, on the global CC characterized also by the rise of HW phenomena, as one of the most relevant effect at regional scales. During the last decades, despite the slow increase in monthly average temperatures and precipitation, many regions around the world have experienced extreme climate-related events like HW, heavy rainfall, droughts and fires, as most noticeable phenomena linked to CC [1]. The climate simulations reinforce the long-term prediction of the trends increase in the number and intensity of these phenomena related to extremes of climate variability [2, 3]. On cities such phenomena have a bigger impact not only for the highest concentration of inhabitants but also for their accentuation arising from alterations of the local thermal response and of the hydrological cycle, typical of many conurbations with high population densities, lack of green space and concentration of built-up and sealed areas, also in synergy with other impact factors (pollution, anthropogenic heat inputs, ...). Here as vegetated and evaporating soil surfaces are replaced by impervious, low albedo paving and building materials, the reduction in the latent heat flux and parallel increase in the sensible heat leads to the formation of the typical UHI's related to the spatial distribution of thermal response [4], with local maxima of LST (Land Surface Temperature) of the most dense areas of urban fabric rising several degrees over that of the rural surroundings [5, 6, 7, 8]. These concomitant factors may negatively affect the urban environment quality increasing at same time the impact of these climate extrema phenomena on citizen's life level and health, particularly in coincidence with HW, which are currently considered an emerging environmental health concern due to growing number of the linked fatalities [9, 6]. In fact the recent HW phenomena (i.e. in 2003 and 2015) are estimated to have resulted in an increasing number of victims, especially among the elderly and those suffering from specific diseases in various parts of the world and also in the countries of Europe bordering the Mediterranean. Here during the HW event of the summer of 2003, warmer than the past 500 years, for several days the average daily temperatures have been higher by various degrees compared with those of previous years, and the values in the months of July and August grew up to 10 ° above the average, with a maximum in France and in Italian central and northern areas[10]. These factors have had a major impact on the health of citizens in Europe, with increase in deaths (over 50,000) attributable to these extreme meteo-climatic events , concentrated mainly in the cities[11, 2]. In order to prevent and minimize these potential negative consequences of these extreme events related to the CC, there are ongoing activities of analysis and research to support interventions and policies concerning mitigation and adaptation in urban areas [12], even in the context of Smart Cities nationals and EU research programs.

The present research work aimed at developing methods for the morphological and typological urban settlements characterization related to these climate aspects associated to the temperature and hydrology (HW, UHI, water cycle, radiative balance,...). In particular the focus was on the evaluation of contribution to the local LST increase from typological, geometric and structural aspects of the city urban fabric whose development is subject to decision-makers policies and administrative planning in the framework of local and national mitigation strategies and adaptation to CC [13]. In this context innovative spatially explicit approaches are increasingly required for obtaining suitable information and for assessing the expected impacts of these meteo-climatic factors at appropriate

 doi:10.20944/preprints201608.0202.v2

spatial and temporal scales, in order to suitably support detailed local plans for increasing the resilience of urban areas in the perspective of prevention, mitigation and adaptation strategies to these phenomena [14].

Many authors dealt with urban fabric characterization for different purposes using remote sensing active and passive HR techniques coupled with visual interpretation and various semi-automatic clustering algorithms and schemas. In general the estimated features of built up refer to its broad classes or general characteristics like impervious surfaces, or urban density classes of urban areas [15, 16], but in general there are very few works based on the exploitation of field assessed attributes of specific built up typologies. Given that the built up is one the most representative element of the urban fabric, our original approach attempted to model its thermal and heat storage properties in terms of those derived for the specific buildings typologies and for the density of their geometric arrangement along the network road (compactness), in our areas of interest. In addition to these built up parameters, firstly derived from photointerpretation supported by field and design information, also the percentage of permeable/vegetated surfaces for each urbanistic parcel was considered significant for fine-scale radiative balance and heat storage capacity [17], which are closely related to UHI formation and vulnerability contribution to HW. Since the results of this semi empirical model based on the above described approach, happened visually reliable at transect level it was then exploited in term of built-up morpho-typological classes as training set for obtaining their distribution for the entire municipality of Rome using an on purpose implemented object based classification supervised procedure. The Landsat 7 ETM+ HR data acquired in 2003 were suitably preprocessed for retrieving ground reflectances under form of spectral indices, tasseled cap components and textures parameters as basic variables more linked to urban surfaces physical properties and tridimensional structure driving the heat exchanges and radiative balance. The obtained distribution of these classes synthetizing the thermal responses of built up components of urban fabric was then exploited for a vulnerability model calibration using the night UHI LST distribution derived from the MODIS satellite products acquired during the HW period of 2003.

Here the information provided by the recent passive remote sensing techniques at medium (i.e. NASA MODIS dual satellite system with daily and night acquisition capability) and high (i.e. Landsat and Sentinel 2 operated respectively by NASA and ESA within the European Copernicus program) integrated by GIS (Geographical Information Systems) ground resolution were exploited for methodology development. The object analysis methods and data mining techniques were suitably integrated for developing the main semi-automatic procedures [17], with the additional goal of improving the standardization and operative aspects, repeatability as well as validation capability of implemented models. In general, the "data mining" term refers to methods, tools and procedures based on statistic, modelling, visual and graphical approaches, to extract useful knowledge from large amount of data usually under form of big datasets (Data-Warehouse).

2. Materials and Methods

Taking into account that on Rome the typical UHI LST distributions usually occur during the nights, in summer, as in other towns of Mediterranean basin [19, 20], the basic idea was to use the related TIR frames detected by MODIS sensors during the 2003 summer, in coincidence with the well-established HW situation [19]. In this perspective the Landsat HR multispectral data were preliminary processed through object classification and data mining procedures to assess the distribution of built-up morpho-typologies over the entire territory of the Rome municipality on the basis of training classes found within the transect area and characterized for their temperature response in the preliminary photointerpretation step. In the Figure 1 the general data processing flow schema was reported. Here the implemented procedure is divided into three main box referring respectively to the photointerpretation phase, the object oriented classification procedure and finally to the MODIS LST models calibration. Here the main processing step of each block are

Preprints (www.preprints.org) | NOT PEER-REVIEWED | Posted: 26 October 2021 doi:10.20944/preprints201608.0202.v2

synthetically indicated while their detailed description and explanation were provided in the following devoted chapters.

The VHR (Very High Resolution) satellite (i.e. WorldView, QuickBird, RapidEye,..) remote sensing techniques (multispectral spatial resolution between 1 and 5 m.), working on commercial basis and based on user specific acquisition request , have been frequently employed to map the fine scale spectral heterogeneity of materials usually present within urban settlements [21, 22]. Due to their favorable spatial/spectral and operative features, also the 30 m. HR multispectral data provided by the Landsat multispectral sensors have been used for retrieving the urban LUCC (Land Use Cover Changes) classes and the concentration of impervious surfaces [23, 24], by means of vegetation and other spectral indices [25, 26, 27] or aerial photos[28], while others authors dealt with supervised classification algorithms testing on urban areas, using different approach including those per pixel and object oriented ones [22, 27].

The Landsat family satellite HR sensors are conceived for systematic acquisitions of reflectance data in seven acquisition bands from 180x180 Km. tiles over entire Earth surface with typical GSR (Ground Sampling Resolution) of 30 m. Starting from the ETM+ on board of Landsat 7 satellite launched on 2000, the GSR was improved by adding a panchromatic channel at 15 m. Thus in the implemented methodology developed on the basis of previous results [29, 30, 31], these panchromatic data having higher GSR were used in synergy with the related multispectral ones with the goal of improving the detection capability of the finer scale textural features of urban fabric.

In the subsequent calibration/validation step a statistical analysis by means of regression modeling was carried out through the exploitation of LST distributions corresponding to know HW periods in summer 2003 and the local nocturnal UHI maxima, frequently occurring over Rome [15] , as told before. In such a way we were able to assess the impact of both these phenomena often acting in synergy to deteriorate the urban microclimate conditions. The HW and UHI phenomena affect the LST distribution which may be derived from thermal infrared (TIR) remotely sensed images having an important role urban studies due to the potentially large-area and repetitive nature of their coverage. Besides the local topography and impervious soil surfaces concentration [12], numerous RS-based UHI studies have suggested the dependence of spatial patterns of intra-city LST, from various attributes of urban area of interest like population [32], land use/cover [33], vegetation coverage [34], anthropogenic heat and urban fabric features [32], not at building typology level. The TIR data are acquired from different polar and geostationary platforms e.g. Landsat, Terra/Aqua MODIS, ASTER, NOAA AVHRR and Meteosat SEVIRI. Although the Landsat sensors are able to detect only the LST diurnal distribution through the TIR acquisition channel (~10-12 μ) at 60 m. of GSR, according to similar applications [32, 34], in this study the Terra MODIS sensor was selected since it is able to provide nighttime data for studying the nocturnal LST distribution, typical of UHI of Rome and others European cities. MODIS LST products (MYD11A1-MODIS/Aqua Land Surface Temperature and Emissivity Daily L3 Global 1 km Grid SIN) even with lower spatial resolution (1 Km.), are particularly suitable for the LST product due their easy availability, global coverage and high calibration accuracy of multiple thermal and other spectral bands.

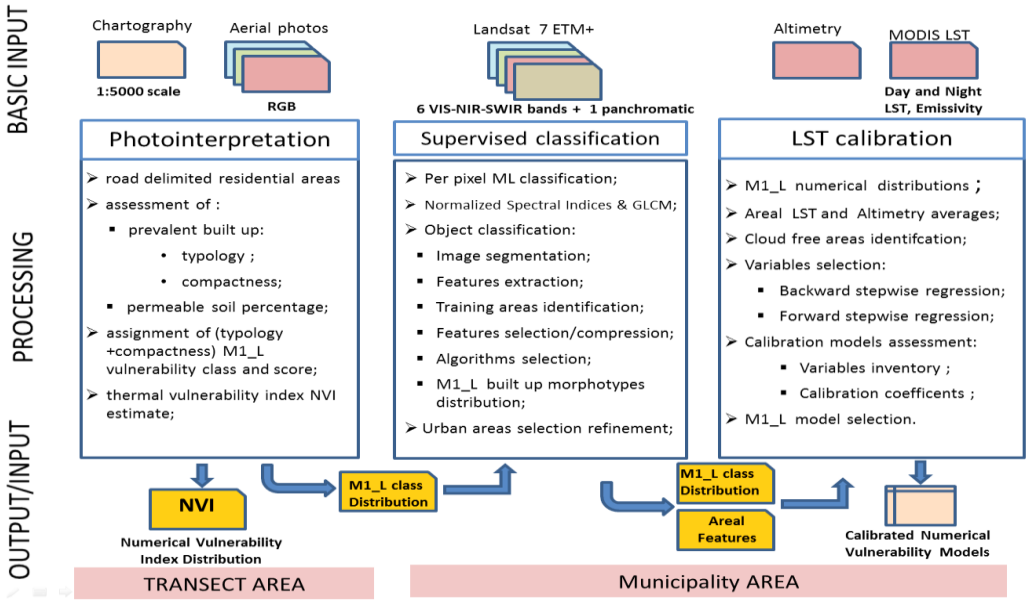

Figure 1 ee main blocks ɔy means of data ı

Preprints (www.preprints.org) | NOT PEER-REVIEWED | Posted: 26 October 2021 doi:10.20944/preprints201608.0202.v2

This calibration procedure allows to properly take into account the atmospheric effects (split window water-vapor atmospheric correction) and emissivity of earth surfaces; furthermore the validation of version 3 standard products from Terra MODIS data shows that their accuracy is better than 1 C° in the range from -10 to +50 C° [35, 36, 37].

2.1. Area of interest

The Rome territory is located in the central Italy (Figure 2) , characterized by Mediterranean climate and annual daily mean temperature of 20°, with its 1.287 Kmq and about 2.875.000 inhabitants it represents the biggest municipality in terms of area and population at European level. Although the Rome municipality includes many protected and green areas, parks and rural landscapes, the huge concentration of historical monuments and cultural heritage coupled with

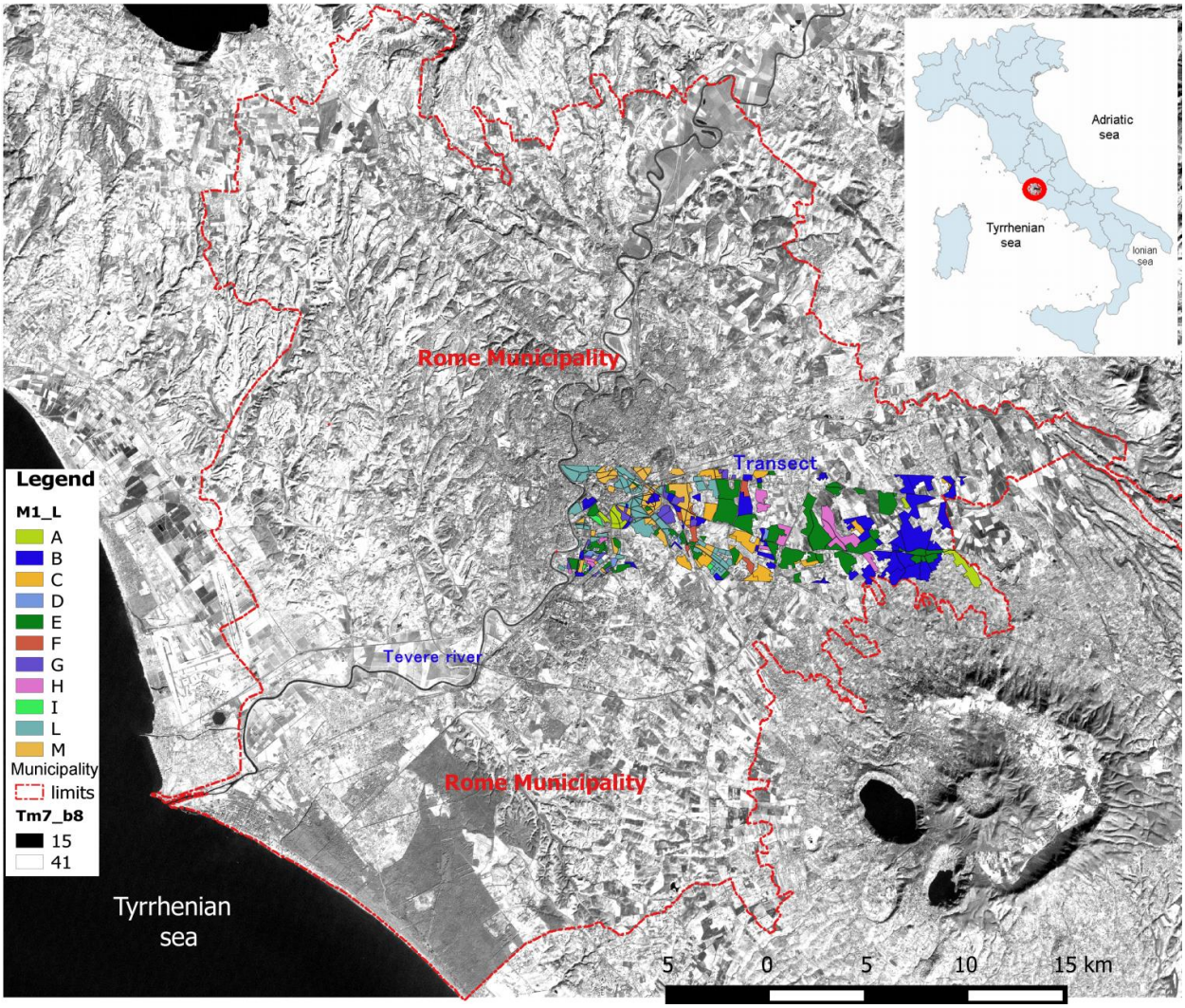

Figure 2 - Area of interest including the Rome municipality territory and M1-L built up morpho-typological classes (coloured polygonals) within the transect derived from photointerpretation methodology . The various vector features were superimposed to orto-rectified panchromatic channel of the Landsat ETM+

pronounced urban sprawl of the recent decades and consequent widening of transportation network and infrastructures, often without an appropriate planning, increase the urbanized zones potentially subjected to impacts and pressures deriving from urban environment quality deterioration arising from ongoing CC and anthropogenic factors.

Although with an average maximum temperature above 30 ° C, the Roman summer was already very hot, in the last decades it has undergone further transformations with a demonstrable

Preprints (www.preprints.org) | NOT PEER-REVIEWED | Posted: 26 October 2021 doi:10.20944/preprints201608.0202.v2

increase in the frequency and intensity of HW and temperature levels (day and night) rise with consequent uncomfortable conditions of malaise for human health. The center of Rome is, roughly, 25 km far from the Tyrrhenian coast. In summer, the moderating influence of the Tyrrhenian Sea is more noticeable on the western slopes of the city, thanks to the local characteristic wind from west to east inhibiting the excessive heat of summer afternoons and relieving discomfort. The situation is different at the center, only partially achieved by this air flow due to heavy urbanization, with temperatures which can record up to 3-4 ° C higher than the western side. Even warmer is the eastern districts, which happens almost entirely without a suitable air circulation.

The average annual precipitation was around 692 mm to the end of the 80s while currently is raising about 750 mm. During the summer, the humidity and high temperatures combined with a modest infiltration of fresh air from the north is the spark that frequently bursts storms of intensity almost unknown in the past.

2.2. Photointerpretation

The initial goal of the work was the photointerpretation-based characterization of the various areas of the transect, homogeneous from the urbanistic point of view and previously identified and delimited on the basis of the existing road network and cartography at appropriate scale (Figure 3). The work was accomplished by assigning to each polygonal area the quantitative attributes derived from the building type and density and from the vegetation/permeable surfaces presence, linked to their hydrological and thermal potential response to the HW and UHI. This approach aimed at the evaluation of a numerical vulnerability index (NVI) for each of the areas, including the cumulative effect of these three main factors related to urban fabric features and estimated with theirs relative scores preliminarily introduced on a semi-empirical basis. Starting from established knowledge and specific urbanistic studies on the urban areas of interest [38, 39], three reference variables were defined: typology and compactness, related specifically to built-up portion of the area and the permeability of the surrounding surfaces. For each of them, on the basis of different relative weights, increasing degrees of partial vulnerability (scores) were assigned through photo interpretation methods. Finally, the NVI estimation for each area of the transect, was derived by summarizing the partial contributions arising from the three variables scores. The 291 polygonal of urban residential areas found in the transect, previously identified using the road network, were thus characterized by photo-interpretation approach in terms of the prevalent buildings typology within 11 predefined types and related compactness level, as the number of floors and mean width/density of contiguous streets, in addition, their percentage of permeable surfaces. In order to assess the global thermal response as NVI of the urban fabric areas inside the transect the quantitative contribution of the three parameters was evaluated in term of intensity levels (score) within a fixed scale of a linear model defined by relative weights (Table 1) and empirically introduced to account for their specific impact in term of local temperature augmentation and related uncertainty:

1. predominant type of buildings within 11 types defined and characterized on the basis of previous studies and knowledge [38], grouped within 6 score classes as reported in Table 2;
2. compactness of the urban fabric, 4 classes: high, medium-high, medium-low, low, with relative scores as reported in Table 1;
3. presence of permeable surfaces, 3 classes: low, medium, high, with relative scores as shown in Table 1, vegetation included, was also visually estimated.

levels of percent relative score	**1**	**2**	**3**	**4**	**5**	**6**	**max score %**
Typology	2	4	6	8	10	20	20
Compactness	5	10	20	35			35
Permeability	1	20	45				45

Table 1- Urban fabric parameters and related score classes for NVI assessment.

Preprints (www.preprints.org) | NOT PEER-REVIEWED | Posted: 26 October 2021 doi:10.20944/preprints201608.0202.v2

The NVI distribution appears to have rightly a negative gradient going from the center to the periphery. Obviously this result is mostly determined by the parameters relating to impervious surfaces and compactness that have similar trends except for some peripheral areas subject to special or intensive urban deployment.

The 11 building typologies were associated with the relative photo-interpreted levels of compactness, for a total of 11 "morpho-types" (Table 3) classes (M1_L) found in the transect (Figure 2, 3), with a summed score in the range from 7 to 45, which synthesizes the specific partial thermal response of built-up and building fraction (Figure 3 b). Due to specificity of the urban fabric of this territory (supported by on field data) not all possible combination of typology and compactness parameters have been represented M1_L classes. Subsequently, for each area in the transect, the scores within the 11 morpho-type classes was added to the corresponding score referring to the permeability parameter, obtaining a distribution of NVI rightly increasing going from suburbs to the more vulnerable downtown zones (Figure 3, a).

n	Typology	class	score
1	building	1	2
2	detached house	1	2
3	line	2	4
4	array	2	4
5	palace	3	6
6	spontaneous	3	6
7	block	4	8
8	semi-intensive	5	10
9	intensive	5	10
10	articulated	6	20
11	tower	6	20

Table 1 - Building typologies and related score classes.

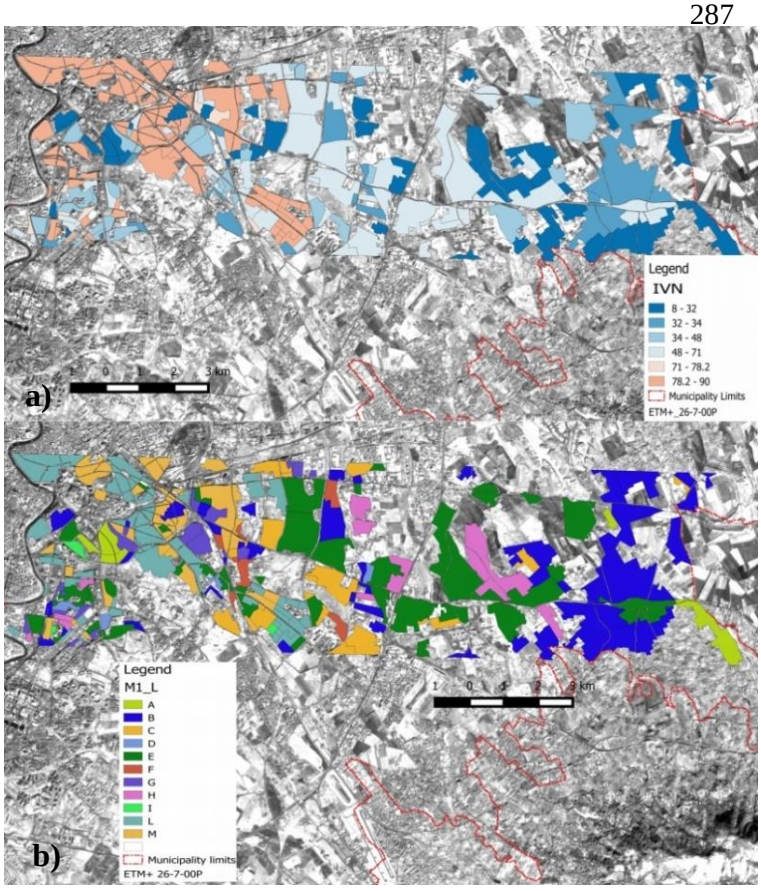

Figure 3 - Detailed transect distribution of the 11 classes of partial vulnerability of the urban fabric morpho-types M1_L (b) and overall vulnerability NVI (a). In overlay panchromatic channel of Landsat ETM+ acquired on 7/27/2003.

M1_L class	Score	Pol. n.
A	7	8
B	12	55
C	16	19
D	18	5
E	22	54
F	26	6
G	28	19
H	30	11
I	37	3
L	43	63
M	45	48

Table 3 - Urban fabric built-up morpho-types (typology+compactness) classes and related score.

Thus the NVI was calculated

 doi:10.20944/preprints201608.0202.v2

according to a simple linear semi-empirical model, that is, by performing the arithmetic sum of the partial contributions of the class levels corresponding to each of the three photo-interpreted features as specific vulnerability factors appropriately scaled according to the relative weight as reported in Table 1 and 3.

2.3. Supervised classification

The objective of this stage was the assessment of the distribution of the urban morpho-typologies found within the transect over entire territory of the Rome municipality through on purpose implemented integrated methodologies based mainly on supervised object classification. The automatic land use/cover classification of urban areas using remotely sensed digital imagery is a particularly challenging task due to their high spectral heterogeneity arising from the mixing of natural and impervious artificial surfaces delimiting urban 3-D elements, like buildings, infrastructures, roads, and parking lots whose spectral responses may be generally too similar to be suitably separated using only the limited information derived from single pixels of the remotely sensed multispectral raster images. Therefore often additional information, are required for improving the discrimination of these land covers by the classifier. To this end the object-based schemas, respects to those pixel-based, provide a more effective way to derive and integrate into the classification process other kind of data related to morphology and context of contiguous pixels groups, preliminarily extracted from the same imagery through segmentation process. In this context to increase the effectiveness of spectral classification semi-automatic approaches, many authors successfully exploited the object-based image analysis methods for properly describing and quantifying the typical spatial heterogeneity of urban land covers using the HR/VHR remotely sensed data [21, 40, 41]. These objects classification approaches in the supervised schemas allowed them to better discriminate multi-pixels ground land-use patches containing a variable mix of different built materials, infrastructures and natural land cover features [42], on the basis of a subset of limited training object preliminarily characterized through visual interpretation or in situ data. These patches (objects) including a variable number of pixels having different spectral signatures work as pre-defined object boundaries, preliminarily obtained through segmentation algorithms based on predefined spectral and geometric parameters (i.e. scale/dimension, spectral homogeneity, textures parameters, convexity,..). In the implemented methodology (Fig. 4) various data mining methods were exploited to properly handle the different spectral and textural components (features) extracted from the Landsat ETM+ multispectral data under form of spectral (SI & tasseled cap), texture and GLCM (Gray Level Co-occurrence Matrix) indices to be used as independent variables in the subsequent modelling and classification steps. In our classification schema the results of object-based method were then refined on the basis of those obtained from a pixel-based one with the objective to provide a more accurate discrimination of urbanized areas of Rome municipality to which is focused the present work.

2.3.1. Data processing schema

The classification procedure implemented with the goal of recognizing the M1_L built up classes over the Rome municipality encompass various interconnected processing steps whose central engine is a supervised classifier trained with the results of photointerpretation at transects level. The Figure 4 shows the logic schema of the procedure including the pre-processing and classification blocks where the processes and data are symbolically indicated and linked together according to the included legend. The main goal of preprocessing was to transform the spectral responses detected by ETM+ orbital sensor (TOA) into signals more linked to the physical properties of surfaces and objects on the earth surface both from radiometric and geometric point of view. In this perspective first of all the ETM+ TOA reflectances (LDS8) data were firstly corrected for removal of the atmospheric noise using an “image based” land oriented approach [64]. Then the corrected reflectance responses in the six acquisition bands of the sensor were transformed into three normalized spectral indices and first three tasseled cap components (brightness, greenness and wetness) [62, 63], which have been introduced to take better into account the spectral properties of

 doi:10.20944/preprints201608.0202.v2

surface covers of interest affecting the radiative balance and heat exchange, in particular built up, vegetated and impervious ones. Another aspect considered in preprocessing was the texture features of urbanized areas with the objective of quantifying the urban fabric compactness parameter previously used in the photointerpretation semi-empiric model. Taking advantage of its improved ground resolution (15 m.) more suitable for capturing the typical built up texture patterns, the atmospherically corrected reflectance data of ETM+ panchromatic channel were processed to extract various texture features. In particular five first order (data range, mean, variance, entropy, skewness) and eight second order(mean, variance, homogeneity, contrast, dissimilarity, entropy, second moment, correlation) GLCM(Gray Level Co-occurrence Matrices) texture metrics were derived using a 5x5 kernel and a -1, 1 shift vector for GLCM [60, 61], all have been stitched in a raster multilayer of 13 co-registered strata. The objective to derive these texture variables at pre-processing level was twofold, not only to provide these relevant information for segmentation process but also to allow a more efficient extraction of GLCM texture directional urban fabric patterns in combination with the other GLCM texture responses (three) automatically derived by the feature extractor (Table 4) using perpendicular shift (1,1) and different kernel (3x3) parameters, as described in the next paragraphs. A principal component transformation of the 13 textures metrics multilayer file was performed in order to produce a four first components including the 85% of variance to be used more efficiently in the subsequent preprocessing steps. Thus in addition to the three spectral indices (SI) and three tasseled cap components also the above first four principal components of texture metrics were provided in input as 10 multilayer raster to the segmentation process where the pixels of the area of interest seen by the satellite sensor are geometrically aggregated on the basis the clusters obtained by means of selected algorithm and recognized as single objects detected on earth surface. With this objective, after various tests, a region growing algorithm based on spectral euclidean distance [44] was selected and tuned to obtain results compatible on average with polygonal areas used in photo-interpretation of the transect and consisting of a vector layer of 4499 polygonal objects covering the entire territory of Rome. For each of them, a set of 196 independent variables, as spectral and GLCM textures were then extracted from the 10 indices multilayer (30 m. of ground resolution) and panchromatic channel (10 m. of ground resolution) as polygonal features (segmentation & feature extraction) and suitably recorded in the related attributes database. In particular, for each raster in the 10 indices multilayer the 9 variable indicated in the table 4 were derived both with their normalized version for a total of 180 while the others 16 were derived from panchromatic band.

The subsequent step of the preprocessing phase was the Maximum Likelihood (ML) supervised per pixel classification of urban areas from the Landsat 7 ETM+ multispectral image corresponding to Rome municipality of previously extracted from the entire frame using a limits polygonal. The training set was derived from the photointerpreted transect data and available certified urban covers (CLC 2006, Urban Atlas) to obtain an urban distribution to be used to further refine the object classification results. The accuracy was assessed by means of the confusion matrix in term of % overall accuracy (OA). The global agreement of the obtained map of urbanized areas with the CLC 2006 (Corinne Land Cover) urban thematic layer was about 85%. From the obtained urban thematic map a percent of urban cover was derived for each segmented polygonal and added as additional attribute. At the end of this preprocessing stage, the segmented cover database included for each of its 3478 polygons, the extracted features (70), the photointerpretation class M1_L value (only the 104 training polygons) and the percentage of urbanization obtained from the area identified by the by pixel classification as attributes.

In the subsequent step (training area identification) the vector layer containing the 291 polygonal of the transect, classified by means of the above described photointerpretation approach, were integrated with the spectral and texture features previously extracted for the segmented layer. Subsequently this upgraded layer was exploited as training/validation data to test preprocessing and machine learning algorithm for morpho-types M1_L classification before to extend the most performant chain to the remaining segmented urbanized 3478 polygonal areas. In the classification stage the M1_L label was assigned to all the polygonal of the segmented cover on the basis of that of

Preprints (www.preprints.org) | NOT PEER-REVIEWED | Posted: 26 October 2021 doi:10.20944/preprints201608.0202.v2

the training ones using the preselected object classification algorithms and features reduction/compression. A successive refinement of the result was carried out by selecting those polygonal with a minimum of urbanized areas found trough previous per pixel classification. Following the typical data mining approaches, the algorithm selection and feature data reduction techniques were previously selected among the most effective [45], on the basis of the results in terms of overall accuracy (OA) and error rate (ER) values obtained using the training set within the comprehensive selection method. The final results as M1_L class cover, including 1539 classified object polygonal with M1_L label, obtained using one of the previously selected algorithms and spectral features input data set are displayed in Figure 7. In the next paragraphs firstly the features implementation and train data extraction were widely described then the selection processes referring to feature reduction and object classification by means of data mining algorithms were explained too.

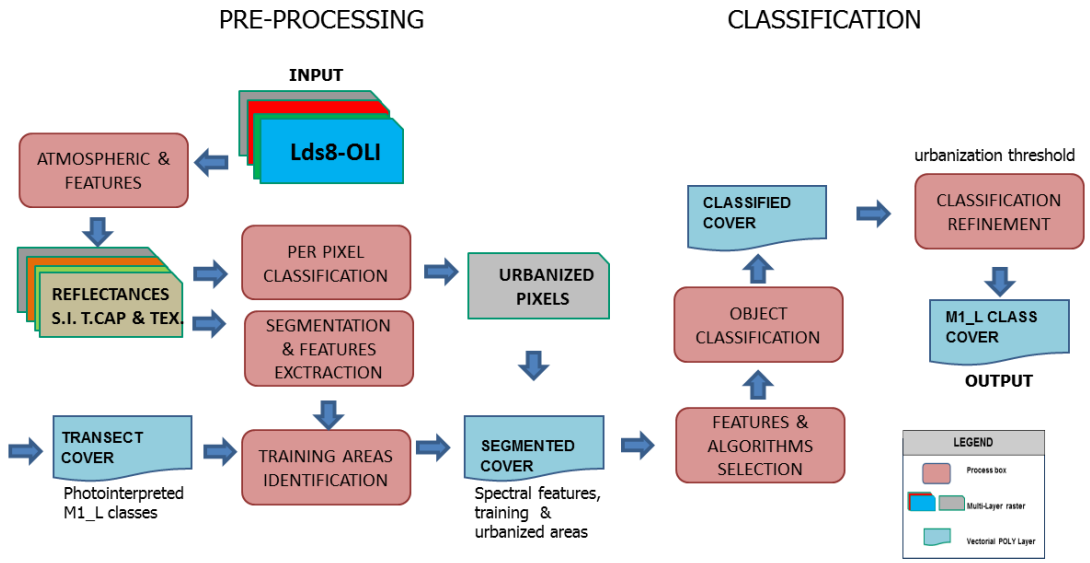

Figure 4 – Schema of Data processing and Object classification of urban fabric morpho-types in the municipality of Rome

2.3.2. *Features and training data*

Considering that the Landsat 7 ETM+, starting from the middle of 2003, suffered from the SLC (Scan Line Corrector) subsystem failure which determined degradation of images acquired after the end of May, with introduction of some gaps without useful data [46, 47], more dense at borders, one of the last good frames acquired on 18 of March 2003, before the SLC damage was processed for the morpho-typologies distribution assessment through object-classification procedure. Such an approach allowed us to extend the knowledge about urban fabric thermal response gained by means of photointerpretation methods on polygonal (objects) of the transect to the other 3400 polygonal objects previously obtained by means of semiautomatic segmentation and covering the entire territory of interest. This was accomplished through advanced clustering data mining algorithms [22, 41], using the 70 spectral-spatial variables suitably extracted from Landsat reflectance data, mostly under form of devoted spectral indices and including those more linked to local textural content [48], as proxy of built-up compactness, introduced in the following.

First of all, to reduce the basic variables number in view of the subsequent object-oriented/data mining approach trying to maintain their useful information contents, the 30 m. TOA (Top Of

 doi:10.20944/preprints201608.0202.v2

Atmosphere) reflectance signals acquired in the six bands were transformed into three normalized spectral indices (SI), more linked to spectral properties of the natural (i.e. vegetation,…) and artificial surfaces of interest [49] and, at same time, to reduce the noise contribution associated to the varying topography and atmosphere:

$$NDVI=(R_4-R_3)/(R_4+R_3) \quad (1)$$

$$NBUI=(R_6-R_5)/(R_5+R_6) \quad (2)$$

$$NDGI=(R_3-R_2)/(R_2+R_3) \quad (3)$$

where, according to Landsat ETM+ sensor spectral configuration, Rn state for reflectance in the nth acquisition band. Bands n. 1,2,3 are respectively the RGB visible channels, while the remaining indicate those in NIR (4) and SWIR (5,6) ranges.

The NDVI (Normalized Difference Vegetation Index) derived from red and NIR (Near Infrared) reflectance signals characterizing the photosynthetic vegetation, was designed for more effectively capturing their spatial and temporal changes. It was widely used for vegetal ecosystems monitoring, in particular it was exploited for usefully assessing various important biophysical parameters of plants linked to their biomass, productivity and health and for studying grasslands and rangelands since the early applications of the satellite EO, starting from the late of the 1970 [50]. According to various authors who subsequently employed this index as proxy of impervious surface density [25, 49], and of surface emissivity for assessing the LST distribution at urban level [51, 52, 53], the NDVI was exploited as proxy of the previously introduced permeability variable and in synergy with the others variable/features for objects characterizing in terms of built up typology and density variables using also the related textural features. Although the NBUI index is less common than NDVI, it was successfully exploited for enhancing the specific spectral responses of building and artificial surfaces detected by remote sensors [43, 49], while the remaining index NDGI was introduced to recover the green spectral response fraction considering the high reflectance of urbanized infrastructures in the visible range and taking advantage from its normalized ratio formulation. The cover of polygonal objects spreading over entire municipality territory has been obtained from these three-indices raster layer through the M. Baatz segmentation algorithm [35], using an appropriate combination of the related input parameters (i.e. scale, color and compactness) preliminarily tuned to produce objects enough compatible in term of size with those previously found into the transect using the visual estimation.

Thus, following the object oriented typical approach the features extraction has been accomplished using both the three indices layer (30 m. GSR) and the ETM+ panchromatic channel (15 m. GSR) for providing to each segmented polygonal object its own attributes synthetizing the spectral and textural features of the corresponding areas to be used as independent variables in the following supervised classification procedures. In addition to the usual spectral reflectance amplitude, mean, mode, standard deviation, sum and ratio also the three first moment GLCM dissimilarity, entropy and homogeneity [48, 49], have been extracted from the four raster layers (three indices + panchromatic) at different GSR using a 3x3 kernel window and predefined offset vector. The ratio variable was calculated only for the three indices layer as pixels sum of fractions of the current component while the amplitude include the intensity difference between maximum and minimum reflectance signal within every polygonal object. The table n. 4 shows the inventory of the nine features/variables extracted for every polygonal object using the available raster layers, including those referring to GLCM domain which have been introduced with the objective to better

Preprints (www.preprints.org) | NOT PEER-REVIEWED | Posted: 26 October 2021 doi:10.20944/preprints201608.0202.v2

capture the local texture features of the urban fabric. In particular the three GLCM variables are: dissimilarity (*Dis*), entropy (*Ent*) and homogeneity (*Hom*). The related pixel values were derived through the respective formulas:

$$Dis = \sum_{i=1}^{D-1} \sum_{j=1}^{D-1} p_{ij} (i - j) \quad (4)$$

$$Ent = -\sum_{i=1}^{D-1} \sum_{j=1}^{D-1} p_{ij} \log p_{ij} \quad (5)$$

$$Hom = \sum_{i=1}^{D-1} \sum_{j=1}^{D-1} \frac{p_{ij}}{1+(i-j)^2} \quad (6)$$

where the p_{ij} is the normalized number of intensity co-occurrences within the kernel, i and j subscripts indicate the gray level (intensity of the component) considered while D is their range corresponding to the dimension of the related GLCM square matrix derived from the number of intensity levels considered. The values of these GLCM variables have been firstly calculated at pixel level using the adopted kernel and offset vector while their mean over polygonal object area was then assumed for the related feature variable. *Dis* is a measurement of the intensity difference between the elements of the GLCM and it is high when the kernel region has a high contrast (i.e. repetitive high building strips and related shadows characterizing dense urban fabric areas). The *Ent* variable measures the local disorder in the distribution of pixel intensities, it increases as they don't happen in regular patterns and many GLCM elements have small values. *Hom* assumes higher values for smaller differences in the GLCM and little differences in local intensity pattern. The nine object variables indicated in table 4, were derived from each of the three above defined normalized indices, stitched in the 30 m. GRS raster layer, while only eight features (ratio excluded) have been calculated from the panchromatic channel. These raster layers have been exploited for assessing the three raster GLCM features which were then averaged for every polygonal object. The obtained set of 35 variables has been doubled by adding their normalized versions for a total of 70 feature variables assessed as attributes of polygonal objects. The objective of the subsequent object classification supervised process was to assess the distribution of the M1_L classes over entire Rome municipality using suitable training data set obtained from the transect photointerpretation and the above EO-derived 70 object feature independent variables. The selection of the training areas in the polygonal cover obtained from segmentation on basis of those employed in the transect was the most critical stage of the implemented method, since the previous ones, being delimited by road network weren't generally exactly coincident with the results of automatic segmentation.. Thus, in order to overcome this difficulty, first of all the segmented polygonal crossing those photo-interpreted in the transect were identified, using the available GIS topological overlay tools.

N.	Variables	Domain	Description
1	amplitude	Polygon	(Max-Min) Local contrast
2	dissimilarity	Poly(GLCM)	Linked to the intensity contrast of repetitive patterns in the region of interest
3	entropy	Poly(GLCM)	Linked to disordered intensity patterns in the region of interest
4	homogeneity	Poly(GLCM)	Linked to flattened intensity patterns in the region of interest.
5	mean	Polygon	average
6	mode	Polygon	mode

Preprints (www.preprints.org) | NOT PEER-REVIEWED | Posted: 26 October 2021 doi:10.20944/preprints201608.0202.v2

7	ratio	Polygon	normalized component
8	std-dev	Polygon	standard deviation
9	sum	Polygon	sum of components

Table 4 - Feature variables extracted from the raster layers and associated to segmented polygonals objects.

Then for each of them a table of the related M1_L classes area percentages in the transect was produced using the zonal majority GIS function in order to allow the evaluation of the predominant cover class. Finally only the segmented polygonal having a majority class percentage higher than a predefined threshold (mainly up to 70%, 40% for two less populated classes) were retained as training areas.

The Figure 5 shows the cover of the selected training set as colored M1_L classes obtained from the segmented polygonal for a total of 104 areas within or adjacent to the transect. These training areas were obtained by overlaying and spatial processing of the segmented polygonal and the 291 transect polygonal of the 11 morpho-types classes (table 3, Figure 3 b) representative of the thermal response of the urban fabric in the Rome municipality. Considering the heterogeneity of residential areas which include different percentage of built-up mainly characterized by high reflectances in visible bands, in order to improve the characterization at municipality level of the urban polygonal objects, a per pixel classification using standard algorithm (ML) was introduced in order to recognize the internal urbanized pixels and to allow a preliminarily selection of the object polygonal based on a percentage threshold of their built-up surface (Figure 4 – URB process) for subsequent object classification step.

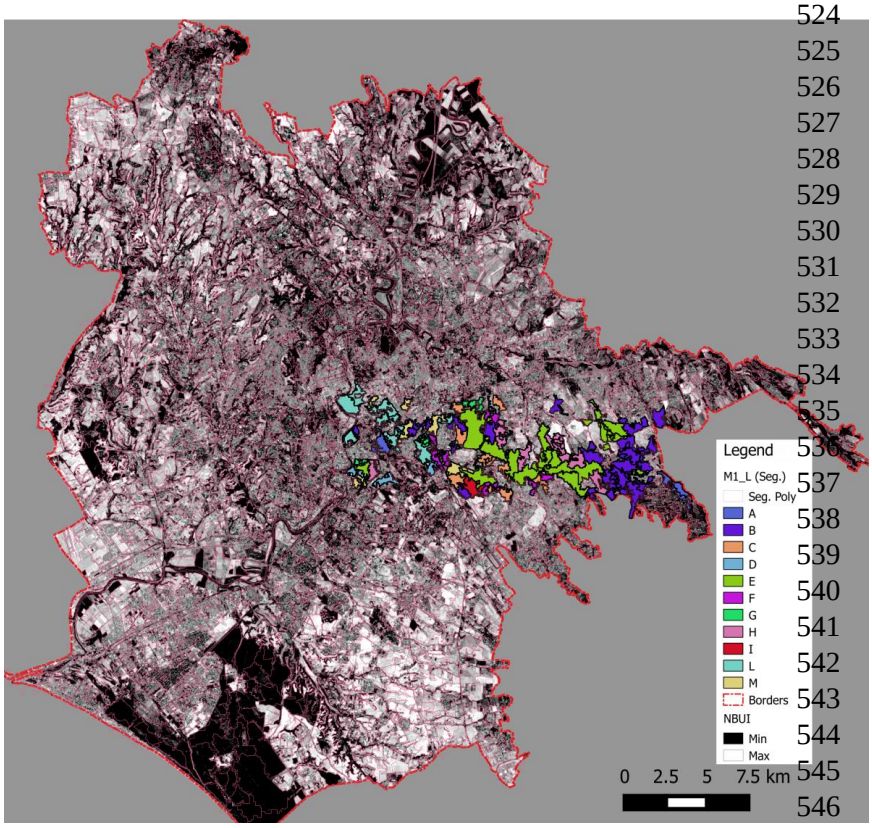

Figure 5 - Urban fabric moprpho-types distribution of training areas within the transect selected from segmented polygonal objects , in overlay to NBUI index distribution at municipality level. Da togliere

2.3.3. Features and algorithm selection

First of all, five typical machine learning algorithms were preliminarily selected for supervised object classification taking into account their different capabilities and performance in various situation of noise, limited class samples and outliers presence in input data: C4.5 (decision tree) , C-SVC (Support Vector Machine- discrete class, continuous input), Knn (K-nearest neighbors), ANN (Artificial Neural Network), RnTr (Random Forest Tree). Decision Tree allows to implement easy to interpret classification models by hierarchically splitting the data set [54, 55]. This algorithm

Preprints (www.preprints.org) | NOT PEER-REVIEWED | Posted: 26 October 2021 doi:10.20944/preprints201608.0202.v2

finds the best subset of attributes based on an entropy measure and organizes the classes in a decision tree rule-based structure. Each node of the tree relates to a split in the feature space which is always orthogonal to its axes. Support Vector Machines, more often used in the per-pixel classification context, is a sophisticated non-parametric supervised statistical learning technique, robust against outliers, that estimates a repartition hyperplane of the feature space that minimizes misclassifications [55, 56]. The k-nearest neighbor algorithm (Knn) is a method for classifying objects based on closest training examples in an n-dimensional features space. When given an unknown feature pattern the classifier searches the pattern space for the k training tuples that are closest to the unknown one [56]. The ANN non parametric algorithms are based on the neural network concepts and work without assumptions about input data distribution and independency. They learn from the training dataset and build relationships (networks) between input (features) and output nodes (classes) through hidden neurons layer connection weights modulation, a critical issue may be the amount of training occurrences which may be critical in our context [56].

The Random Forest classifier consists of a group of decision trees induced with different sub-sets of the training data. Each tree of the forest casts a vote for the class to which a given analysis unit (in this case, a given segment) should be associated [56, 57]. The class with most votes is the one associated to the segment.

The high dimensionality of the extracted features used as EO-derived input data (i.e. our 70 variables) is potentially affected by a variable level of noise and cross-correlation of the components whose specific contribution may be irrelevant or even detrimental (introducing confusion) in object classification task by means of a particular algorithm. Thus an integrated approach for data reduction and algorithm selection was implemented for improving classes detection and processing efficiency [21], using the previously assessed polygonal training set. Initially the entire training data set containing the feature attributes and related class label for the 104 polygonal was processed in order to assess the accuracy in term of error–rate (ER) derived parameter (1-overall accuracy/100) for each of the algorithm above introduced.

Subsequently only the randomly selected 70% of the data set was exploited for training phase while the test was carried out on remaining samples to evaluate the algorithm overtraining weakness. These last process was repeated three times and the results mean was retained as more representative ER on the basis of cases sampling increase (Table 5). In table 6 was reported the confusion matrix obtained from the classification result of C4.5 applied to the training set. The related overall accuracy (OA) as the fraction of number of correctly labeled objects (evidenced in bold along the principal diagonal) is 0.6538 while the corresponding error rate (ER) is 0.3462. The specific accuracy is varying for each class and drops to 0 for C and D (missed) classes. The following repetitive classification trials of the random selection of 30% of the training set by means of the same C4.5 algorithm, suitably trained with the remaining input data, produced the ER results included in table 6, with related average in the last line. As you can observe, the 65% OA, obtained with the entire training data set, decreases to less than 30%, in case of repetitive train/test classification trials using respectively the 70% and 30% of the training data, while the number of undetected classes rises until 5 (Table 7).

Trial	**Train size**	**Test size**	**Error Rate**	**O.A.**
1	72	32	0.6875	0.3125
2	72	32	0.7188	0.2812
3	72	32	0.6563	0.3437
			0.6875	0.3124

Table 5 - Train/test trials results and related mean (last line).

 doi:10.20944/preprints201608.0202.v2

M1_L class	L	B	C	M	F	G	E	I	H	D	A	Sum
L	6	0	0	2	2	0	1	1	0	0	0	**12**
B	0	20	0	0	2	0	1	0	1	0	0	**24**
C	0	0	0	0	3	0	1	0	4	0	0	**8**
M	0	1	0	4	0	2	0	0	0	0	0	**7**
F	0	0	0	0	6	1	1	0	0	0	0	**8**
G	0	0	0	0	0	3	1	0	0	0	0	**4**
E	0	1	0	0	0	0	15	2	1	0	0	**19**
I	0	0	0	1	0	0	0	3	0	0	0	**4**
H	0	0	0	0	0	1	0	0	8	0	0	**9**
D	0	2	0	0	1	0	0	0	0	0	2	**5**
A	0	1	0	0	0	0	0	0	0	0	3	**4**
Sum	**6**	**25**	**0**	**7**	**14**	**7**	**20**	**6**	**14**	**0**	**5**	**104**

Table 6 – Confusion/contingency matrix derived from object classification of training set using C4.5 decision tree algorithm.

The above described two steps tests were then carried out using the others algorithms above introduced. Then, according to general data-mining approach, two different methods for input data reduction were applied to the training set:

- the transformation of data to a lower dimensionality by means of the PCA (Principal Component Analysis) data transformation [56];
- the selection of most significant features, termed feature selection, using different statistical techniques, namely: Fischer; Run Filt; Step.

The output of the PCA transformation of the original 70 features data set were uncorrelated components retaining a decreasing portion of the global variance, as depicted in figure 6. As you can see here, more than 90% of variance of the initial data set is preserved if we consider the first 21 PCA components instead of the original 70 variables. While the PCA transform input feature by mixing them on the basis of their mutual correlation, the feature selection methods allow to select a features subset from the original set without any transformation, and maintains the physical meanings of the original features. Even if, in this sense, feature selection is superior in terms of better readability and interpretability, here, in addition to the standard ones, we tried to apply in sequence these two approach (i.e. the feature selection was applied also to the PCA components). Starting from the feature attributes of the 104 polygonal in the training set whose dimensionality makes impossible the selection by means of the usual manual approach on the basis of visual comparison of distribution and multidimensional scatter plots, three techniques representative of the automatic continuous feature selection for for classification labelling were exploited. Thus the Fisher, Runfilt and Stepdisk [21, 56, 57], were then introduced with the aim to select a smaller subset of input data minimizing their redundancy and maximizing relevance to the target scope, such as the suitable class labeling, in classification. The first two methods are based on the filter model which is independent from the subsequent learning algorithm and considers only the general characteristics of the training data such as distance, consistency, dependency and information content for assessing the input feature quality. STEPDISC (Stepwise Discriminant Analysis) exploits a discriminant analysis criterion. Others approach (wrapper, embedded) include the specific classifier algorithm in input feature selection and weren't considered here since this step was in any case performed subsequently in our procedure. The feature selection step was applied also to the subset of the selected PCA components, with the objective to find the most linked with the classes of training set. Ultimately all combinations relating to five different algorithms, two training/test approach and

 doi:10.20944/preprints201608.0202.v2

feature selection techniques were tested for assessing their global accuracy in term of ER (O.A.) values which are arranged in the two following tables n. 7 and 8. In particular, the first table n. 7 includes the results obtained using the features of training set while the second one shows the ER's assessed for the subset of the first 21 PCA components, containing an amount higher than 90% of the original explained variance (Figure 5).

The first two lines of table n. 7 report the ER values obtained from classification of the training set using the five algorithms above introduced with all 70 features. The first one refers to the entire data set (all-70) while the second include the result for the related train/test approach (all-T). Similarly, in the following two row, the result of the feature selection using the Fisher filtering method are reported respectively for the selected data set including the first most relevant 35 components (35) and related train/test evaluations (35-T). The same schema is repeated for the remaining features selection methods applied here and in the subsequent table referring to PCA components. The "Feature n." columns (corresponding to different three selection techniques) of the two tables indicate the number of selected components while the T suffix state for train/test evaluation. All the resulting ER values are reported with a following number in brackets which indicates the missed classes (null accuracy) in classification, except those corresponding to detection of all the classes without brackets. Due to its structural overfitting aptitude some not

	Features n.	**C4.5**	**C-SVC**	**Knn**	**ANN**	**RnTr**
	all -70	0.3462 (2)	**0.1635**	0.5192 (1)	0.4519 (6)	
Sel. Tech.	all-T	0.7188 (5)	0.7292(5)	0.7500(5)	0.6875(5)	0.7917 (5)
	35	0.3365 (1)	0.3462	0.4615	0.5000(6)	
Fisher	35-T	0.7396 (6)	0.7396(5)	**0.6563 (3)**	0.7604 (7)	0.7188 (4)
	35	0.3558 (2)	0.3173	0.4712	0.5192 (6)	
RunFilt	35-T	0.7396 (6)	0.6563(4)	0.6979 (3)	0.7500 (8)	0.7396 (4)
	35	0.3365 (2)	0.3077	0.5192 (2)	0.5192 (5)	
Step	35-T	**0.6250(5)**	0.7292(4)	0.6667 (3)	0.6875 (8)	0.7604 (3)

Table 7 - ER values obtained from classification of the original and reduced training data sets

significant results corresponding to RnTr algorithm aren't included. The most relevant ER values referenced in the following are shown in bold digit. In general the number of the selected descriptors/features with different methods is depending on their relevance/correlation with the training classes distribution assessed trough ANOVA analysis and F-test on the basis of predefined threshold.

In our case a number of selected features corresponding approximately to one half of the original one was adopted in order to provide reduction factor (50%) for enough effective performance evaluation of the various combination of selection techniques and algorithms. As shown in the two first rows of table n. 7, although the ER obtained by C-SVC algorithm seems the best (lowest) in classifying the complete training set, its relative performance significantly decreases in test case (all-T second row) , in which all the results happen poor, with a relevant number (5 on average) of missed classes. The results of the C4.5 classifier improve with the feature subset selected using the Fisher and Step techniques even in the train/test trials, while those obtained by the Knn algorithm with Fisher selected data set might represent an optimal trade-off between the minor ER value and number of missed classes, both with selected dataset (no missed classes) and in train/test trial.

Preprints (www.preprints.org) | NOT PEER-REVIEWED | Posted: 26 October 2021 doi:10.20944/preprints201608.0202.v2

		C4.5	C-SVC	Knn	ANN	RnTr
	Pc21	0.4423 (4)	0.4808(1)	0.5288 (1)	0.5769 (7)	
Sel. Tech.	Pc21-T	0.7813 (6)	0.7477(6)	0.7917(7)	0.7292(7)	0.8333 (5)
	10	0.4519 (5)	0.5385(4)	0.5288(1)	0.6154(8)	
Fisher	10-T	0.8021 (6)	**0.6563(7)**	0.7708 (6)	0.7813 (8)	0.8021 (4)
	10	0.4231 (2)	0.5577(4)	0.5481	0.6154 (7)	
RunFilt	10-T	0.7604 (6)	**0.6354(7)**	0.7604 (3)	0.8021 (8)	**0.6979 (4)**
	10	0.4615 (2)	0.5577(5)	**0.5192**	0.6442 (8)	
Step	10-T	0.7604(7)	0.7396(7)	0.8125(7)	0.8125 (8)	0.7917 (7)

Table 8 - ER values obtained from classification of the PCA- compressed and reduced training data sets

The test results of Table 8 obtained with Pc21, PCA-compressed data set at the 90% of explained variance, are generally a bit poorer than the corresponding values of Table 7, except for the ER values derived for the Step selection using the Knn classifier which outperform also that related to Pc21 compressed dataset lowering at same time the missed classes number. Finally, considering the ER values/missed classes numbers obtained using the different selection techniques on the entire data set and the capability to be robust against overtraining by means of the train/test approach, firstly the 35-features data set derived through Fischer method and Knn classifier were exploited for the subsequent classification step of the global dataset of the 3478 polygonal objects, covering the entire municipal area. From the results reported in table 7, due to their performance in terms of ER / missed classes amount and/or robustness against overtraining, two additional classifiers, namely C4.5 and C-SVC respectively with Fisher-selected and all features, were also considered. These three alternative M1_L distributions indicated as KnnF (Knn classifier with features Fisher selection) , C4.5S (C4.5 with Stepwise selection) and C-SVC (using all features), obtained from the above classification algorithms were preliminarily selected. The obtained thematic map referring to the former C-SVC is reported in Figure 7. The in depth evaluation for refining their selection was performed in the subsequent LST based calibration phase through their corresponding numerical sliced counterparts indicated respectively as KnnFN, C4.5SN and C-SVCN and obtained by assigning the relative class scores included in table 3.

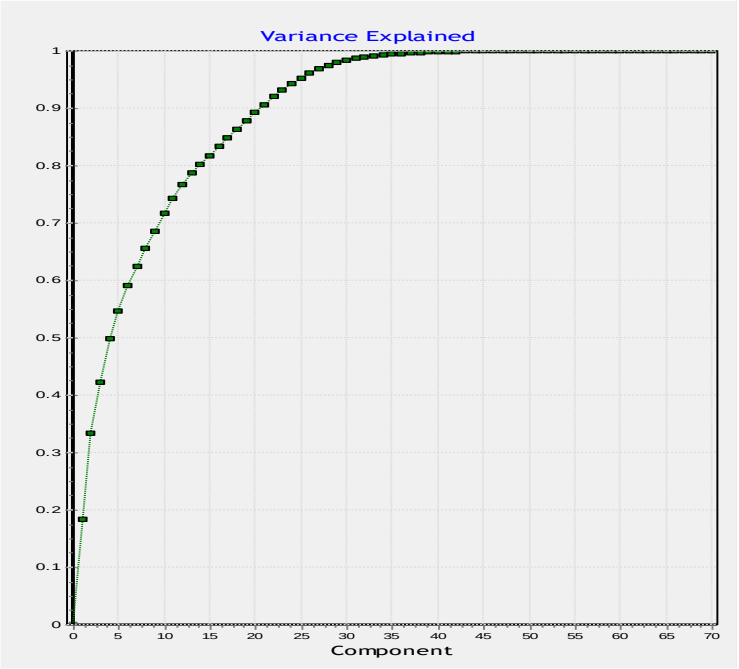

Figure 6 - PCA components and the related cumulative normalized amount of the explained variance

 doi:10.20944/preprints201608.0202.v2

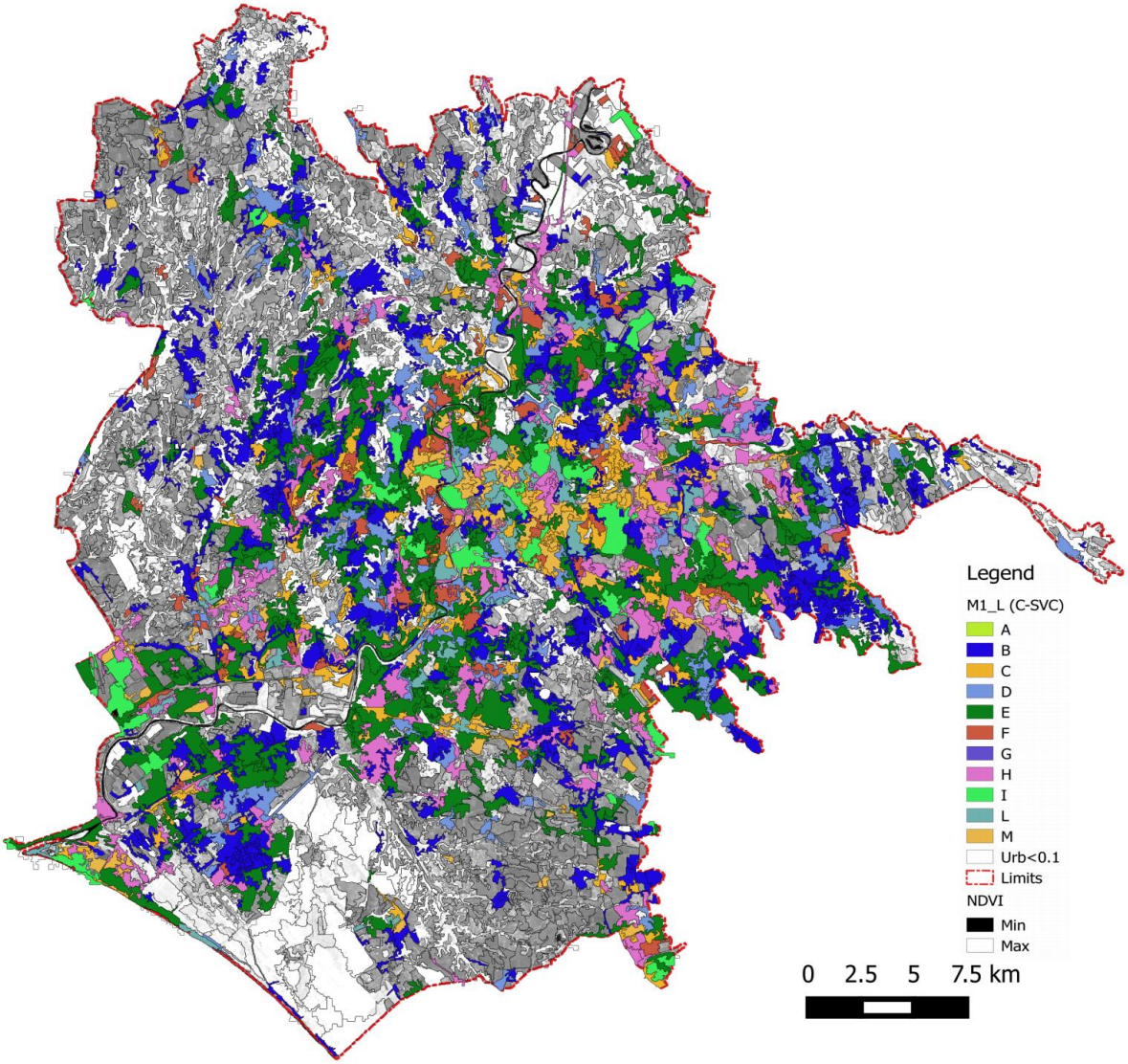

Figure 7 - M1_L classes distribution on Rome municipality territory obtained by means of the implemented supervised object classification procedure through C-SVC algorithm using the transect training areas. The classified polygonal (colored) are superimposed to NDVI distribution (gray scale) at municipality level.

2.4. LST calibration

The preliminary NVI distribution at municipality level might be obtained from the numerical distributions of M1_L urban fabric partial vulnerability classes, provided by object classification procedure, and corresponding NDVI as permeability proxy, but it is affected by some uncertainties and concerns arising from:

- the use the best M1_L distribution within the three previously selected for optimizing different parameters;
- the relative weights between the different factors in the NVI semi empirical model (exploited at transect level), are assumed without a sufficiently robust physical basis.

In order to better address these weaknesses of the photointerpretation based approach, the basic idea was to exploit the LST distributions measured in HW and UHI condition for a physically based model calibration. Given that the HW and UHI synergy reflects on the LST distribution as the main measurable effect, it is assumed as dependent variable of a multivariate regression model whose independent variables have to be selected within the most significant of all the previously

Preprints (www.preprints.org) | NOT PEER-REVIEWED | Posted: 26 October 2021 doi:10.20944/preprints201608.0202.v2

extracted object features. The three M1_L numerical distributions, previously obtained from the classification procedure were added with the local altimetry to the independent variables data set before the selection for a total of 74 independent variables of a multivariate model to be optimized by selecting the more significant variables using step-wise regression statistical methods. All the (dependent and independent) model variables at polygonal level were arranged to provide a unique data set for the 1539 classified urban objects which was then exploited for variable selection and model calibration using the stepwise regression methods as described in the following. In this perspective, two typical LST distributions of Rome nocturnal UHI, captured by MODIS polar satellite sensor in the summer 2003 (Figure 8), were selected as input to the physically based calibration method of the urban fabric vulnerability M1_L model, previously introduced on empirical basis. The LST distributions refer to the HW period of July 2003 and are reported in the figure 8 (left and right pictures). Here you can see how the night LST distribution in the leftmost and rightmost images exhibit local UHI maxima in correspondence of the town center while the central diurnal image of the 16-7-2003 is characterized by a diffuse cloud cover which decrease the detected radiant temperature over land. Although the cloud presence has decreased in coincidence of the night acquisition (right image) some mist residuals have remained on the right borders of the municipality corresponding to mountains areas and coinciding with colder patch.

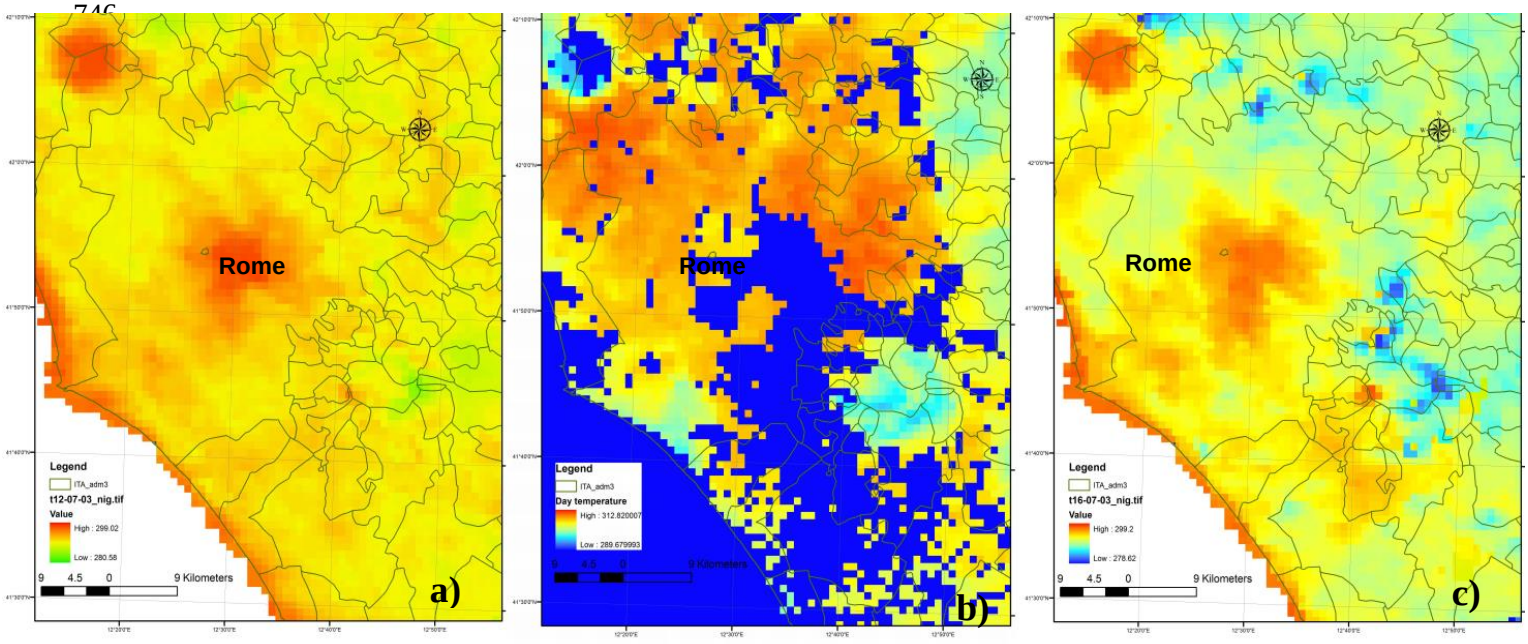

Figure 8 - LST distribution on Rome municipality acquired by MODIS sensor in 12-7-2003 at 21.30 (a) and in 16-7-2003 at 09.30 (b) and 21.30 (c).

In the following graph of figure 9 the bi-spectral plot of the two night LST distribution of 12 and 16 July 2003 related to the polygonal objects corresponding to different M1_L classes are reported. Here you can see how the unreliable lowest temperatures corresponding mainly to these residual cloudiness affect the distributions, in particular that of the 16-07 which required a preventive selection of the cloud free and most reliable polygonal areas to be used in variable selection.

The polygonal samples have been selected trying to exclude the clouds artifacts and according to a temperature threshold (285 T°) compatible with reliable summer (see x-LST value of graph on Figure 9) land values. The graph of Figure 9 displays the bi-spectral plot of the mean LST assessed for each segmented polygonal from the MODIS distributions referring to nights of 16-7-2003 (x-axis) and 12-07-2003 (y-axis). The different point symbols of polygonal LST distribution indicate the various M1_L classes obtained by C4.5S classifier. The colder polygonal affected by cloud cover of the 16-07-2003 were removed using the previous threshold to select the distribution portion

Preprints (www.preprints.org) | NOT PEER-REVIEWED | Posted: 26 October 2021 doi:10.20944/preprints201608.0202.v2

included in the box (dashed red border) at the upper right corner of the graph for the subsequent stepwise analysis.

The objective of the stepwise methods introduction here was to assess a regression model by selecting only the most relevant variables within those available (74) and possibly including as few variables as possible because each irrelevant regressor decreases the precision of the estimated model coefficients and predicted values.

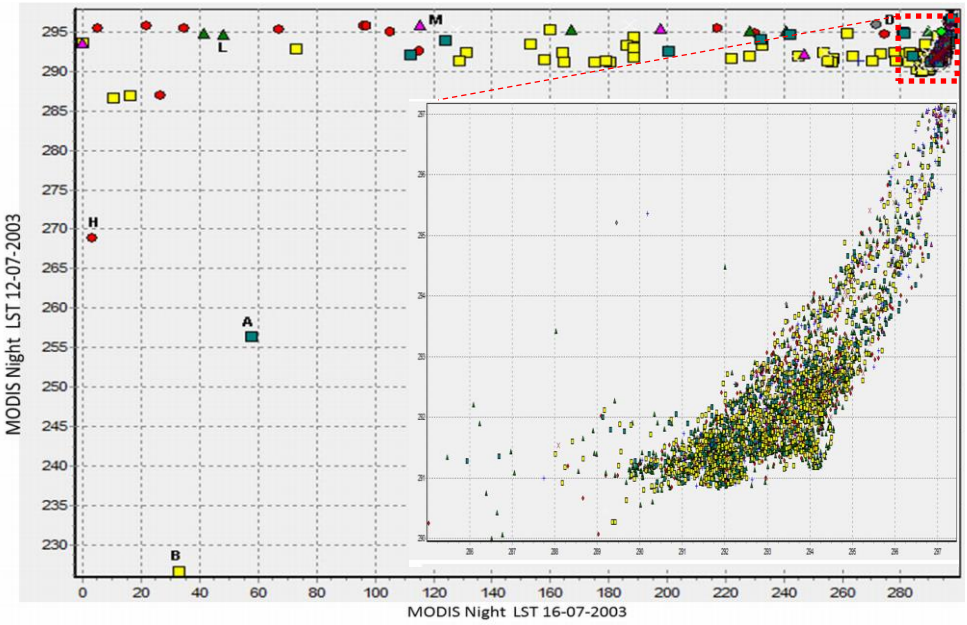

Figure 9 - Bi-spectral plot of the LST (T°) distribution of 16-07-2003 vs that of 12-07-03 inside the segmented polygonal objects whose M1_L class obtained using the C-SVC classifier is indicated using different point symbols. The graph on the right side shows the zoomed distribution inside the red dashed box in the upper right corner with reduced point symbols.

The detailed graph on the lower right side refer to the qualitative distribution in the interval of the 16-07-2003 LST, selected to avoid cloud noise effects. In such a way both the selection of the most appropriate variables including those related to the previous NVI transect model and estimate of the related weights (coefficients of regression model) were achieved on the basis of the LST distributions. In the stepwise method the variables selection for the regression model is carried out by successively adding (forward) or removing (backward) variables based solely on the t-statistics of their estimated regression coefficients [58]. The stepwise option lets you either begin with no variables in the model and proceed forward (adding one variable at a time), or start with all potential variables in the model and proceed backward (removing one variable at a time) based on the previously selected thresholds for the coefficients. In the table n. 9 a synthesis of the results obtained through backward (Bck) and forward (Frw) stepwise regression application with the two above described LST distributions is reported. The number of selected variables (N° var.) with related significance level (Sig. lev.) of t- statistics threshold used for inclusion/exclusion and the estimated coefficients for the most significant of them in the assessed multivariate models are included in the table. As reported in Table 9, both the C4.5SN and C-SVCN independent variables, derived from M1_L, are relevant in explaining the LST spatial distribution especially in models obtained from the forward stepwise method, which include the NDVI index and a minor number of independent variables (8) for the LST distribution detected in two different dates during the HW period. Finally the R^2 correlation levels ranging from 0.472 to 0.27, and F/p-value parameters are also included to highlight the models significance.

Preprints (www.preprints.org) | NOT PEER-REVIEWED | Posted: 26 October 2021 doi:10.20944/preprints201608.0202.v2

Although the four models contain different independent variables here firstly we focused on those previously introduced for estimating NVI at transect level related to urban fabric features and soil permeability. Since these formers, namely the M1_L numeric distributions and NDVI, as soil permeability proxy, are selected in all models their importance in determining the thermal response of urban fabric was confirmed . First of all it should be evidenced that the both C4.5SN and C-SVCN numerical urban fabric partial vulnerability distribution have been retained in the estimated models while the KnnF variable, despite its good statistical performance with variables selection, didn't agree enough with the considered HW-UHI LST patches.

	LST-12-07-2003		LST-16-07-2003	
	Bck	**Frw**	**Bck**	**Frw**
Sig. Lev.	0.1	0.0001	0.1	0.0001
N° var.	16	8	16	8
C4.5SN		0.013969	0.010265	0.006966
C-SVCN	0.011381	0.021581		0.014668
KnnFN				
NDVI-mean	-0.08302	-0.05773		-0.03360
NzNDVI-mean			-7.964	
NzPan_mode		0.0000001		0.0000001
R^2	0.477	0.38	0.362	0.28
R^2_{adj}	**0.472**	**0.377**	**0.354**	**0.276**
n. samp.	1534	1534	1262	1262
F	869.912	1176.056	442.863	611.608

Table 9 - Backward (Bck) and forward (Frw) stepwise results for multivariate regression models of the two night LST distribution on Rome territory during the HW of 2003

The increasing contribution of urban fabric M1_L distributions to temperature rise is evidenced by the related coefficient sign which maintain positive in all models while the opposite sign corresponding to NDVI is related to cooling effects arising from the permeability and vegetation increase. In agreement with the general indications in our case although the estimated models using the backward method exhibit higher correlation coefficients (Table 9) they include more numerous significant independent variables which make difficult the physical explanation of their connection with the LST distribution. Thus given that the forward procedure is generally retained more suitable to provide an initial screening of the candidate variables within a large group and also for its robustness against the multicollinearity and outliers problems [59] the corresponding results are considered for the M1_L distribution selection. reported. In Table 10 and 11 all the independent variables of the complete models selected via forward stepwise for the Rome night LST distribution of the 12 and 16 July 2003 are In addition to M1_L numeric distributions previously introduced, the others independent variables included are referenced using names with suffixes and prefixes assigned by the segmentation and data mining software packages previously exploited in features extraction and object classification procedure. In particular the prefixes indicate the three previously introduced normalized spectral indices(respectively NDVI, NBUI and NDGI), while nz, pn, pnz state correspondingly for

Variable	**Coef.**	**std**	**t(1529)**	**p-value**
Intercept	297.430.196	0.529670	561.538.321	0.000000
C4.5SN	0.013969	0.005345	2.613.432	0.008952
NDGI-ratio	12.252.723	0.608251	20.144.190	0.000000
NDVI-mean	-0.057728	0.003120	-18.503.385	0.000000
nz_NDVI-ratio	5.478.326	0.748758	7.316.554	0.000000
C-SVCN	0.021581	0.003839	5.622.098	0.000000
pnz_mode	0.000000	0.000000	-5.186.027	0.000000
NBUI-amp	0.004156	0.000760	5.465.880	0.000000
nz_NBUI-mode	0.000000	0.000000	4.634.898	0.000004

Table 10 - Regression model obtained by means of the forward stepwise variable selection for the LST night distribution of 16-07-2003.

Preprints (www.preprints.org) | NOT PEER-REVIEWED | Posted: 26 October 2021 doi:10.20944/preprints201608.0202.v2

normalized polygonal average, panchromatic and panchromatic normalized polygonal average. The suffixes are introduced according to variables names reported in Table 4.

Variable	Coef.	std	t(1253)	p-value
Intercept	303.454.833	0.740549	409.770.309	0.000000
C4.5-SN	0.006966	0.005457	1.276.643	0.201963
NBUI-mean	-0.020506	0.001413	-14.514.235	0.000000
NDVI_mean	-0.035626	0.002516	-14.160.640	0.000000
pnz_mode	0.000000	0.000000	-7.614.581	0.000000
nz_NDGI-amp	0.706314	0.143912	4.907.956	0.000001
pn_mode	-0.007164	0.001757	-4.077.290	0.000048
NBUI-Ent	0.000900	0.000231	3.904.598	0.000099
C-SVCN	0.014668	0.003932	3.730.728	0.000199

Table 11 - Regression model obtained by means of the forward stepwise variable selection for the LST night distribution of 12-07-2003.

The selected variables for the model of the night LST distribution captured by MODIS sensor on the 12-07-2003, as the previous one, comprise the same two M1_L numeric distributions, polygonal means of the NDVI and NBUI indices, and panchromatic channel normalized mode (pnz_mode). Differently from the model referring to the LST distribution of the more cloudy night of 16-07-2003, here other variables were included namely the normalized amplitude of NDGI (nz_NDGI-amp), the polygonal mode of panchromatic channel (pn_mode) and the NBUI GLCM entropy (NBUI-Ent). In both the models the forward selection included the two M1_L C4.5-SN and C-SVCN numeric distributions referring to urban fabric features previously assessed by means of photointerpretation methods. In addition also the NDVI related mean and pnz_mode polygonal variables were selected in both the LST models.

3. Results and discussion

A semi-empirical linear model of thermal vulnerability of urban areas, based on built up characteristics and presence of permeable surfaces/vegetation was firstly implemented in order to quantitatively estimate the contribution of the urban fabric features related to temperature extrema regional meteo-climatic phenomena even in synergy with the well-known UHI local anomalies. The built up features focused for this purpose have been the building/infrastructure typology and compactness which were further characterized in term of classes and related numerical grades/scores on the basis of preexisting knowledge and studies on the various urban areas of Rome. This semi-empirical model was applied to a 20x5 km. transect test area through its preliminarily road-delimited residential urbanistic homogeneous areas, using mainly an on purpose developed photointerpretation method of large scale detailed cartography. In such a way the preliminary distribution of thermal vulnerability M1_L classes (Figure 2) and related scores coming only from urban fabric was produced. The association of the numerical scores assigned to M1_L distribution with those derived from photo-interpreted permeable surface percentages for each of the previously introduced residential areas allowed us to obtain a preliminary and qualitatively reliable, thermal vulnerability distribution under form of NVI (Numerical Vulnerability Index) at transect level (Figure 2). Trying to extend these preliminaries results obtained in the transect area to entire municipality of Rome a semi-automatic methodology based on the remotely sensed data exploitation was conceived with the goal to detect the different M1_L classes on the basis of their spectral and textural features increasing at same time the efficiency, reliability, generality and applicability of the method. The implemented methodology consists in a original procedure based on integration between per pixel and object supervised

 doi:10.20944/preprints201608.0202.v2

classification steps working on polygonal objects preliminarily obtained for the entire municipal territory using a widely used multispectral segmentation algorithm. In addition to panchromatic channel three normalized spectral indices derived from Landsat ETM+ multispectral images were exploited as basic input data, with the objective to enhance the vegetation and built up typical reflectance responses, minimizing at same time the noise contribution from atmosphere and illumination sharp variations from cast shadows of buildings. In particular the usual NDVI linked to vegetation density was introduced as robust proxy of area permeability while NBUI was retained more linked to built-up typology and compactness. To improve the discrimination of these different fundamental characteristics of urban fabric, in particular those linked to built-up typology/compactness, also the spectral texture related indices derived from GLCM obtained from multispectral and panchromatic data were also included. In such a way a total of 70 independent variables were assessed for each of the 3400 polygonal areas obtained from segmentation and covering the entire municipality territory. A training set of 104 areas was then extracted from these polygonal by overlaying them with those exploited in the photointerpretation of transect features and using spatial GIS analysis to evaluate the majority M1_L univocal class of each of them. This step was very problematic, especially for some M1_L classes represented by too small and fragmented areas at transect level which often spread over different segmented polygonal without any prevalent class area percentage. It should be underlined also that some of these difficult classes are less representative, due their typologies (i.e. tower) including too few examples, important only for their architectural particularity. The training set of these segmented labeled polygonal and related attribute values of 70 variables was exploited to select both the best data-mining algorithms and related feature selection/compression strategies on the basis of their performance in term different accuracy and train suitability parameters. Following the general data-mining approach to deal with a big amount of input information, three classification algorithms and related input data handling strategies were selected according to their capabilities to optimize different aspects, let's say the classification accuracy in term of O.A. / ER, the number of missed M1_L classes and the robustness against overtraining. The subsequent object classification by means of the selected combination of algorithms and related preprocessed features has been carried out on those segmented polygonal including an urban pixel percentage greater than 10%. The urban pixel distribution was previously assessed by means of an usual per pixel supervised classification using transect training areas, with a general agreement respect to comparable official thematic maps of urban areas (i.e. Urban Atlas, CLC 2006) provided by EEA(European Environment Agency) . According to the NVI semi-empirical linear model used at transect level, to quantitatively assess the thermal vulnerability for the entire territory of interest, the obtained distributions of M1_L built up classes were transformed into their numerical counterparts using the table 3 and associated with NDVI index polygonal average, as effective proxy of permeable surface percentages. Conversely, to rightly address the remaining ambiguities about the best M1_L distributions and the subjectivity of model weights which have been previously introduced on the basis of rough knowledge of building material used for different typologies in town districts, a more physically based approach, based on the real UHI night LST distribution captured by MODIS satellite sensors during a HW situation was implemented. Thus four models for 12-07-2003 and 16-07-2003 LST distributions were assessed using the three obtained M1_L numerical distribution, altimetry and the 70 polygonal attributes as independent variables input which were then selected by means of backward and forward stepwise regression procedures. The statistical parameters reported in table 9, show that all the estimated models give a noticeable contribution to variance of the LST spatial distribution with adjusted correlation (R^2_{adj}) going from 0.47 to 0.28 and confidence level higher than 99%. The results of backward stepwise procedures include models with a greater number of independent variables and higher correlation than those obtained by means of forward ones. Due to less cloud cover the number of cloud-free polygonal referring to LST distribution of 12 July is increased respect to that of 16 July with consequent improvement of correlation and confidence level of the related models. Both the C4.5SN and C-SVCN distributions, as positive contributions to temperature rise (positive coefficients), were included in the models assessed through stepwise

 doi:10.20944/preprints201608.0202.v2

procedures while the KnnFN was excluded with altimetry variable. The NDVI index (always with right negative coefficients) and normalized mode referring to panchromatic channel (pnz_mode) with very small positive coefficient contributed significantly to the LST spatial variance. In the forward model of the 12 July (table 11) the NDVI and NBUI polygonal mode (NDVI_mean, NBUI_mean) and panchromatic mode (pn_mode) provide negative contribution to the LST rise while the positive ones come from M1_L distribution, C4.5-SN and C-SVCN (more statistically significant), normalized panchromatic mode (pnz_rode) and finally from the GLCM entropy derived from NBUI (NBUI_Ent). The NBUI negative contribution could be associated to refrigerating effect from dense street shadows linked to photo-interpreted compactness level while the GLCM entropy could arise from the disordered built up concentration, especially in older city districts lacking of wind and air circulation cooling effects.

Various commercial and open sources packages and software were suitably exploited in integrated way for data processing following the above reported general schema. In particular the ERDAS-Imagine and ENVI commercial suites were used for EO and raster data processing while spatial analysis based mainly on vector coverages have been performed by means of ARC GIS distributed by ESRI inc. and Q-GIS open source tools. Finally TerraView-Geodma and Tanagra freely available software platforms and the commercial E-Cognition package, have been exploited in development of the segmentation and object classification procedures.

4. Conclusion

The cities may be considered sensible areas to HW exposure as one of the CC impacts, their vulnerability assessment in terms of social and physical factors should be spatially assessed and possibly addressed to improve their resilience in the framework of local and national adaptation strategies. In this context the suitable spatial assessment of the thermal behavior of the different urban fabrics is an indispensable knowledge for designing the effective urban regeneration, recover, restoration and development. These activities are widely pursued by local administrations and city architects within their planning and management duties in the perspective of the environmental quality improving and energy saving within the general sustainability policies and EU framework of mitigation and adaptation strategies against the CC. Thus this work was focused on the implementation of an innovative methodology based on the integration of satellite multispectral and multiplatform remote sensing techniques in order to suitably support the extensive and operative characterization of the urban fabric thermal responses to UHI and HW, on the basis of its geometric and typological parameters, coupled with the presence of permeable soil/vegetation. Eleven typologies/compactness different classes of thermal response related to Rome urban fabric, were previously defined and recognized within a road-delimited blocks of 20x5 Km transect test area, using photointerpretation methods. They were then successfully detected over the entire territory of Rome using an on purpose developed automatic procedure, based on the ETM+ remotely sensed HR multispectral data and supervised object classification approach, optimized by means of data mining methods. These former have been introduced for properly handling the significant amount of information connected to the spectral/textural features considered in the object classification approach. Due to increasing availability of EO information provided by more and more advanced remote sensing sensors with improved spatial, radiometric and multi-hyperspectral resolutions, data mining methods are increasingly required to cope with these big-data sets. This procedure includes innovative and original solutions for both classification algorithm selection and optimization of features selection/compression, in addition it includes the synergy of per pixel and objects supervised classification approaches to improve the detection and characterization of urbanized areas based on spectral and texture features.

Finally the physically-based extensive calibration/validation of the thermal vulnerability model of urban fabric, previously introduced on a semi-empirical basis at transect level, was originally accomplished by means of the LST night distributions detected by MODIS satellites sensors during the HW phenomena of the summer 2003 and documented by the historical

series of meteorological and satellite data available, in conjunction with UHI condition, clearly evidenced in the processed frames. In such a way the effective contribution of typology/compactness built-up classes to temperature rise was confirmed and quantified like the mitigation effect of vegetation as proxy of permeable soil through NDVI. From the stepwise regression analysis also the NBUI spectral index, exploited by various authors as proxy of urban density, seemed to be able to capture the probably cooling effect provided by tall buildings shadow. Finally also various spectral and textural features derived from the panchromatic channel at 15 m. of GRS, happened significantly correlated with LST through opposite contributions to be further analyzed in term of their physical meaning and link with urban fabric parameters in a future work. Despite its established importance in LST distribution, the altimetry was non included within the more significant independent variables selected by stepwise algorithms, maybe for its too low variation range and perhaps also for uncertainties introduced in the GIS based selection of the training areas using the road-delimited transect stock areas. This former remains a critical passage in the developed procedure which will require further refinement to be better addressed using, for instance, a preliminary segmentation before the photointerpretation step.

This work was developed in the frame of the Project "RoMA" , funded by Italian MIUR (Ministry of the University and Research), SCN_00064 Call "Smart Cities and Communities".

We would like to thank U.S. Department of the Interior, NASA and U.S. Geological Survey for providing the publically accessible Landsat and MODIS data and product via respectively http://earthexplorer.usgs.gov/ and http://modis.gsfc.nasa.gov/.

Author Contributions: Ombuen S., Barbieri L., Benelli F., Camerata F., Pellegrini V., Filpa A. designed and developed the vulnerability semi-empirical model for providing the built up categorization and photointerpretation of the transect area. Borfecchia F. conceived the basic ideas and overall schema for this study, supervised all the processing steps and wrote the first version of this manuscript. Caiaffa E., Rosato V., Pollino M. implemented all the procedures for spatial analyses based on GIS tools and methods, in addition they accomplished the English language review. De Cecco L., Martini S., La Porta L., performed processing of MODIS and Landsat remotely sensed data.

Conflicts of Interest: The authors declare no conflict of interest.

References

1. Giordano, L.; Giordano ,F.; Grauso S.; Iannetta ,M.; Sciortino, M.; Bonnati , G.; Borfecchia, F. Desertification vulnerability in Sicily. Proc. Of the 2nd Int. Conf. On New Trend in Water and Environmental Engineering for Safety and Life: Eco-Compatible Solution for Aquatic Environments, 2002.

2. Barriopedro, D.; Fischer, E. M.; Luterbacher, J.,; Trigo, R. M.; Garcia-Herrera, R. The hot summer of 2010: Redrawing the temperature record map of Europe', *Science*, 2011, 332(6026), 220–224.

3. EEA Report No 2/2012. Urban adaptation to climate change in Europe, Challenges and opportunities for cities together with supportive national and European policies. SBN 978-92-9213-308-5. doi:10.2800/41895.

4. Borfecchia, F.; De Cecco, L.; Pollino, M.; Martini, S.; La Porta, L.; Zinzi, M.; Carnielo, E. Telerilevamento HR Multispettrale/Lidar e Modellistica SVAT 3d per la stima del bilancio Energetico in Ambiente Urbano. Proc. 15th National Conference ASITA , 2011, 449- 460, ISBN 978-88-903132-6-4. 15-18, Novembre Reggia di Colorno, Parma – Italy.

5. Oke, T.R. The energetic basis of the urban heat island. *Quarterly Journal of the Royal Meteorological Society*, 1982,108(455), 1-24. http://onlinelibrary.wiley.com/doi/10.1002/qj.49710845502/pdf.

6. Arnfield, A. J. Two decades of urban climate research: a review of turbulence, exchanges of energy and water, and the urban heat island. *Int. J. Climatol*. 2003, 23, 1–26.

7. Rajasekar, U.; Weng, Q. Urban heat island monitoring and analysis using a non-parametric model: A case study of Indianapolis. *ISPRS Journal of Photogrammetry and Remote Sensing*, 2009, 64 (1), 86-96.

8. Imhoff, M. L; Zhang, P.; Wolfe, R. E.; Bounoua, L. Remote sensing of the urban heat island effect across biomes in the continental USA. *Remote Sensing of Environment*, 2010, 114, 504–513.

9. Gabriel, KM.; Endlicher WR. Urban and rural mortality rates during heat waves in Berlin and Brandenburg, Germany. *Environmental Pollution*, 2011, 159(8-9), 2044-2050.

10. IPCC, 2012: Managing the Risks of Extreme Events and Disasters to Advance Climate Change Adaptation. A Special Report of Working Groups I and II of the Intergovernmental Panel on Climate Change [Field, C.B., V. Barros, T.F. Stocker, D. Qin, D.J. Dokken, K.L. Ebi, M.D. Mastrandrea, K.J. Mach, G.-K. Plattner, S.K. Allen, M. Tignor, and P.M. Midgley (eds.)]. Cambridge University Press, Cambridge, UK, and New York, NY, USA, pp. 582.

11. Michelozzi, P.; De'Donato, F.; Bisanti, L.; Russo, A.; Cadum, E.; De Maria, M.; D'Ovidio, M.; Costa, G.; Perucci, C. A. The impact of the summer 2003 heat waves on mortality in four Italian cities. *Eurosurveillance, Surveillance report*, 2005, 10 (7), n. 6.

12. Mackey, C.W.; Lee, X.; Smith, R.B. Remotely sensing the cooling effects of city scale efforts to reduce urban heat island. *Building and Environment*, 2012, 49, 348-358.

13. Borfecchia, F. Impatto dei cambiamenti climatici sulle città: ondate di calore e UHI. Il clima cambia le città. In *Strategie di adattamento e mitigazione nella pianificazione urbanistica*. Musco, F.; Zanchini, E. Franco Angeli/Urbanistica, 2014, pp.416 Codice ISBN: 9788820487232.

14. Inostroza, L.; Baur, R.; Csaplovics, E. Urban sprawl and fragmentation in Latin America : A dynamic quantification and characterization of spatial patterns. *Journal of Environmental Management*, 2013, 115, 87-97.

15. Zhou,W.; Cadenasso, M.. L.; Schwarz, K.; Pickett S. T.A. Quantifying Spatial Heterogeneity in Urban Landscapes: Integrating Visual Interpretation and Object-Based Classification. Remote Sens. 2014, 6, 3369-3386; doi:10.3390/rs6043369

16. Myint , S. W.; Gober, P.; Brazel, A.; Grossman-Clarke S.; Weng Q. Per-pixel vs. object-based classification of urban land cover extraction using high spatial resolution imagery. Remote Sensing of Environment, 2011, 115(12), 1145-1161.

17. Zhang; H., Jing, X. M.; Chen J. Y.; Li J. J.; Schwegler, B. Characterizing Urban Fabric Properties and Their Thermal Effect Using QuickBird Image and Landsat 8 Thermal Infrared (TIR) Data: The Case of Downtown Shanghai, China. Remote Sens. 2016, 4, 2256-2276; doi:10.3390/rs4082256.

18. Rakotomalala , R. TANAGRA: a free data mining software for research and academic purposes. Proceedings of European Grid Conference, 2005, RNTI-E-3, 2, 697-702, Amsterdam, February 2005.

19. Fabrizi, R.; Bonafoni, S.; Biondi, R. Satellite and Ground-Based Sensors for the Urban Heat Island Analysis in the City of Rome. *Remote Sens*. 2010, 2(5), 1400-1415; doi:10.3390/rs2051400.

20. Santamouris M. Advances in Building Energy Research, Volume 1, Earthscan. Copyright. London-Sterling – VA, 2007, ISBN 978-1-84407-389-4.

21. Novack, T.; Esch, T.; Kux, H.; Stilla, U. Machine Learning Comparison between WorldView-2 and QuickBird-2-Simulated Imagery Regarding Object-Based Urban Land Cover Classification. *Remote Sens*. 2011, 3, 2263-2282; doi:10.3390/rs3102263.

22. Li, C.; Wang, J.; Wang, L.; Hu, L.; Gong, P. Comparison of Classification Algorithms and Training Sample Sizes in Urban Land Classification with Landsat Thematic Mapper Imagery. *Remote Sens*. 2014, 6, 964-983; doi:10.3390/rs6020964.

23. Michishita, R.; Jiang, Z.; Xu, B. Monitoring two decades of urbanization in the Poyang Lake area, China through spectral unmixing. *Remote Sensing of Environment*, 2012, 117, 3–18.

24. Zhang, Q.; Li, B.; Thau, D.; Moore, R. Building a Better Urban Picture: Combining Day and Night Remote Sensing Imagery. *Remote Sens*. 2015, 7, 11887-11913; doi:10.3390/rs70911887

25. Liu, K.; Su, H.; Zhang, L.; Yang, H.; Zhang, R.; Li, X. Analysis of the Urban Heat Island Effect in Shijiazhuang, China Using Satellite and Airborne Data. *Remote Sens.* 2015, 7, 4804-4833; doi:10.3390/rs70404804

26. Kaspersen, P. S.; Fensholt, R.; Drews, M. Using Landsat Vegetation Indices to Estimate Impervious Surface Fractions for European Cities. *Remote Sens*. 2015, 7, 8224-8249; doi:10.3390/rs70608224.

27. Weng, Q. Remote sensing of impervious surfaces in the urban areas: Requirements, methods, and trends. *Remote Sensing of Environment*, 2012, 117, 34–49.

28. Parece, T. E.; Campbell J. B. Comparing Urban Impervious Surface Identification Using Landsat and High Resolution Aerial Photography. *Remote Sens*. 2013, 5, 4942-4960; doi:10.3390/rs5104942.

29. Scott, D.; Petropoulos, G. P.; Moxley, J.; Malcolm, H. Quantifying the Physical Composition of Urban Morphology throughout Wales Based on the Time Series (1989–2011) Analysis of Landsat TM/ETM+ Images and Supporting GIS Data. *Remote Sens*. 2014, 6, 11731-11752; doi:10.3390/rs61211731.

30. Borfecchia, F.; Caiaffa, E.; Pollino, M.; De Cecco, L.; La Porta, L.; Ombuen, S.; Barbieri, L.; Benelli, F.; Camerata, F.; Pellegrini, V.; Filpa, A. Assessment della vulnerabilità del tessuto urbano a heat waves ed UHI tramite tecniche di Remote Sensing ed object classification,. Proc.18th ASITA Conference, 14-16 Oct. Florence,. 2014, pp. 187–194, ISBN 978-88-903132-9-5.

31. Borfecchia, F.; Rosato, V.; Caiaffa, E.; Pollino, M.; De Cecco, L.; La Porta, L.; Ombuen, S.; Barbieri, L.; Benelli, F.; Camerata, F.; Pellegrin, V.; Filpa, A. Assessing the Urban Fabric Vulnerability To Heat Waves And UHI using Remote Sensing and Object Classification. IEEE International Geoscience & Remote Sensing Symposium, 2015, Catalog Number: CFP15IGA-USB, ISBN: 978-1-4799-7928-8.

32. Wang, J.; Huang, B.; Fu, D.; Atkinson P. M. Spatiotemporal Variation in Surface Urban Heat Island Intensity and Associated Determinants across Major Chinese Cities. *Remote Sens*. 2015, 7, 3670-3689; doi:10.3390/rs70403670.

33. Stathopoulou, M.; Cartalis, C. Daytime urban heat islands from Landsat ETM+ and Corine land cover data: An application to major cities in Greece. *Solar Energy*, 2007, 81, 358–368.

34. Odindi, J. O.; Bangamwabo, V. ; Mutanga, O. Assessing the Value of Urban Green Spaces in Mitigating Multi-Seasonal Urban Heat using MODIS Land SurfaceTemperature (LST) and Landsat 8 data. *Int. J. Environ. Res*. 2015, 9(1):9-18, ISSN: 1735-6865.

35. Keramitsoglou, I.; Kiranoudis, C. T.; Ceriola, G.; Weng, Q.; Rajasekar, U. Identification and analysis of urban surface temperature patterns in Greater Athens, Greece, using MODIS imagery. *Remote Sensing of Environment*, 2011, 115(12), 3080–3090.

36. Wan, Z.; Zhang, Y.; Zhang, Q.; Li, Z. L. Quality assessment and validation of the MODIS global land surface temperature. *Int. J. Remote sensing* , 2004, 25(1), 261–274.

37. Wan Z. New refinements and validation of the MODIS Land-Surface Temperature/Emissivity products. *Remote Sensing of Environment*, 2008, 112, 59–74.

38. D'Onofrio Rosalba, Talia Michele . La rigenerazione urbana alla prova. Franco Angeli Editore. Collana: Urbanistica: Studi urbani e regionali. Marzo 2014. ISBN-13: 978-88-917-0960-8.

39. Filpa, A.; Ombuen, S. Comprendere i cambiamenti climatici. Pianificare per l'adattamento. Understanding climate change. Planning for adaptation,. *Urbanistica*, 2014, 5 (2); ISSN: 1973-9702.

40. Ceccarelli, T.; Smiraglia D.; Bajocco S.; Rinaldo S.; De Angelis A.; Salvati L.; Perini L. Land cover data from Landsat single-date imagery: an approach integrating pixel-based and object-based classifiers. *European Journal of Remote Sensing* , 2013, 46, 699-717.

41. Hussain , M.; Chen, D.; Cheng, A.; Wei, H.; Stanley, D. Change detection from remotely sensed images: From pixel-based to object-based approaches. ISPRS Journal of Photogrammetry and *Remote Sensing* , 2013, 80,91–106.

42. Berger, C.; Voltersen, M.; Hese, S.; Walde, I.; Schmullius, C. Using Geographic Object-Based Image Analysis (Geobia) for Urban Land Cover Mapping and Settlement Density Assessment. Proceedings of the 4th GEOBIA, May 7-9, 2012 - Rio de Janeiro – Brazil, 2012, .503-508.

43. Liu, L.; Zhang, Y. Urban Heat Island Analysis Using the Landsat TM Data and ASTER Data: A Case Study in Hong Kong. *Remote Sens.* 2011, 3, 1535-1552; doi:10.3390/rs3071535.

44. Bins L. S'A., Garcia Fonseca L. M., Erthal G. J., Mitsuo Ii F. Satellite Imagery Segmentation: a region growing approach. ANAIS VIII Simposio Brasileiro de Sensoriamento Remoto, Salvator, Brasil, 14-19 abril 1996, INPE, 677-680.

45. Jungho, I.; Zhenyu, L.; Jinyoung, R.; Lindi, J. Q. Impervious surface quantification using a synthesis of artificial immune networks and decision/regression trees from multi-sensor data, *Remote Sensing of Environment*. 2012, 117, 102–113.

46. Zhang, C.; Li, W.; Travis, D. Gaps-fill of SLC-off Landsat ETM+ satellite image using a geostatistical approach. International Journal of Remote Sensing, 2007, 28, 5103–5122

47. Chen, J.; Zhu, X.; Vogelmann, J. E.; Gao, F.; Jin, S. A simple and effective method for filling gaps in Landsat ETM+ SLC-off images. *Remote Sensing of Environment*, 2011, 115, 1053-1064.

48. Zhang, C.; Li, P.; Wang J. Urban Built-Up Area Extraction from Landsat TM/ETM+ Images Using Spectral Information and Multivariate Texture. *Remote Sens.* 2014, 6, 7339-7359; doi:10.3390/rs6087339.

49. Xu, H. Extraction of Urban Built-up Land Features from Landsat Imagery Using a Thematic oriented Index Combination Technique. Photogrammetric *Engineering & Remote Sensing*, 2007, 73(12), 1380–1391.

50. Todd, S.W.; Hoffer, R.M.; Milchunas D.G. Biomass estimation on grazed and ungrazed rangelands using spectral indices. *International Journal of Remote Sensing*, 1998, 19, 427–438.

51. Salehi, B.; Zhang, Y.; Zhong, M.; Dey, V. Object-Based Classification of Urban Areas Using VHR Imagery and Height Points Ancillary Data. *Remote Sens*. 2012, 4, 2256-2276; doi:10.3390/rs4082256.

52. Zhang, H.; Jing, X. M.; Chen, J. Y.; Li, J. J.; Schwegler, B. Characterizing Urban Fabric Properties and Their Thermal Effect Using QuickBird Image and Landsat 8 Thermal Infrared (TIR) Data: The Case of Downtown Shanghai, China. *Remote Sens*. 2016, 8(7), 541; doi:10.3390/rs8070541.

53. Keramitsoglou, I.; Kiranoudis, C. T.; Ceriola, G.; Weng, Q.; Rajasekar, U. Identification and analysis of urban surface temperature patterns in Greater Athens, Greece, using MODIS imagery. *Remote Sensing of Environment*, 2011, 115(12), 3080–3090.

54. Quinlan, R. C4.5: Programs for Machine Learning; Morgan Kaufmann Publishers: San Mateo, CA, USA, 1993; p. 302.

55. Pinho, C. M. D.; Silva, F. C.; Fonsec, L. M. C.; Monteiro, A. M. V.. Intra-Urban Land Cover Classification From High-Resolution Images Using The C4.5 Algorithm. *The International Archives of the Photogrammetry, Remote Sensing and Spatial Information Sciences*. Vol. XXXVII. Part B7. Beijing ,2008.

56. Wieland, M.; Pittore M., 2014. Performance Evaluation of Machine Learning Algorithms for Urban Pattern Recognition from Multi-spectral Satellite Images. *Remote Sens*. 6, 2912-2939; doi:10.3390/rs6042912.

57. Breiman, L. Random Forests. Machine Learning . 2001, 45 (1), 5–32. doi:10.1023/A:1010933404324.

58. Webb, A. R. Statistical Pattern Recognition. Second Edition, QinetiQ Ltd., Malvern, UK, John Wiley & Sons Ltd, The Atrium, Southern Gate, Chichester, West Sussex PO19 8SQ, England., 2002.

59. Miller, A. Subset Selection in Regression. 2002, Chapman and Hall/CRC, ISBN 9781584881711.

60. Haralick, R. M., Shanmugan, K., and Dinstein, I., 1973. Textural Features for Image Classification. IEEE Transactions on Systems, Man, and Cybernetics, Vol. 3, No. 6, pp. 610-621.

61. M. Herold, Liu X. H., Clarke K. C. Spatial Metrics and Image Texture for Mapping Urban Land Use. *Photogrammetric Engineering & Remote Sensing*, 2003, 69(9), 991–1001.

62. Healey S. P., Cohen W. B., Zhiqiang Y., Krankina O. N. Comparison of Tasseled Cap-based Landsat data structures for use in forest disturbance detection. Remote Sensing of Environment , 2005, 97, 301 – 310.

63. Bolun Li, Chaopu Ti 1, Yongqiang Zhao 1,3 and Xiaoyuan Yan 1,* Estimating Soil Moisture with Landsat Data and Its Application in Extracting the Spatial Distribution of Winter Flooded Paddies. Remote Sens. 2016, 8, 38; doi:10.3390/rs8010038.

64. Richter R., Schlapfer D., Muller A. (2006a). An automatic atmospheric correction algorithm for visible/NIR imagery. Int. J. Remote Sensing, 27, 2077-2085.

 doi:10.20944/preprints201608.0202.v2